Chapter 3

Chromatin fluidity and role of higher order chromatin organization as a structural element of nuclear architecture.

3.1 Summary

The genomic organization in the nucleus of eukaryotic cells is by far the most complex and dynamic self-assembled structure. The entire genome is condensed as chromatin due to the histone protein and DNA interactions. Access to the information on the genome requires "remodeling" of the chromatin, which is spatio-temporally regulated inside the nucleus. A variety of ATP dependent enzymes participate in the remodeling of chromatin, either by charge modifications or by reorganization of the DNA strand on the histone octamer at a single nucleosomal level. The mechanism of the physical reorganization of the nucleosome is poorly understood. In this chapter we have explored a mechanistic basis for chromatin accessibility, where the fluidity of the chromatin is increased due to the disruption of histone tail interactions. We have used the phase sensitive measurements in an intensity modulated optical trap described in the previous chapter, to detect increased fluidity of chromatin due to tension induced decondensation. In this approach the fluctuations in the phase lag of the trapped bead, with respect to the periodic modulation of the trap potential, change with the local solution viscosity. The phase sensitive measurements using the intensity modulated optical trap is described in the methods section 3.3.2. Section 3.4.1 discusses our results on measurement of the fluidity of chromatin when decondensed either by tension induced mechanical rupture of histone tail interactions or by trypsin digestion of histone tails.

A packing ratio of ~10^4-10^5 is achieved in order to organize the genome into a eukaryotic nucleus. The structure of the chromatin and the higher order organization of the chromatin is mediated by the histone terminal regions and other non-histone proteins. The chromatin fiber of persistence length 30nm when present as a random coil would require a volume of 70μm. Higher order condensation leads to efficient packing of the chromatin into the nucleus with a diameter of ~20μm. The condensation of the chromatin is hence important for the structural stability of the nucleus. In our approach we disrupted the chromatin organization by trypsin digestion of histone terminal regions to decondense the chromatin, in nuclei isolated from HeLa cells expressing H2B-EGFP fusion protein. Section 3.4.2 discusses our results on implications of chromatin decondensation on the nuclear stability.

We show that chromatin decompaction resulting from digestion of the chromatin associated proteins and other nuclear scaffold proteins, destabilizes the nucleus. Trypsin digestion on isolated HeLa nuclei decondenses the chromatin leading to nuclear swelling as observed on fluorescence microscope. Nuclear digestion with Clostripain, specific to the histone tails, resulted in similar increase in nuclear volume. We measured the decondensation pressure which results in membrane expansion and eventual nuclear rupture to be ~3kPa using an atomic force cantilever. The nuclear stiffness was found to decrease due to the trypsin induced unfolding of the higher order chromatin organization. We measured the softening of the nucleus by using an optically trapped bead adhered onto the nucleus. The anisotropy of the H2B-EGFP fusion stably transfected into the HeLa cell was measured during trypsin digestion to follow the global decondensation of chromatin and showed a decrease in the mean anisotropy values.

3.2 Introduction

The genome of eukaryotic organisms is condensed into a compact structure called the chromatin, Figure 3.1 [1]. Histone proteins that are highly basic are responsible for condensing the negatively charged DNA polymer through the electrostatic interactions. The core histones, the linker histones and other non-histone proteins participate in condensing genomic DNA into higher order structures, achieving a packing ratio as high as ~10^4 in the mitotic phase of the cell cycle. About 146 base-pair length of DNA is wound around the "histone octamer" to form the fundamental nucleosomal structure. The histone octamer is made up of two copies each of the core histone proteins, H2A, H2B, H3 and H4. The core histone tails that are unstructured do not participate in the structure of the nucleosome core particle; rather they protrude out of the nucleosome [2] and are involved in the organization of nucleosomes into higher order structures [3]. The linker histones that bind at the DNA entry-exit sites of nucleosomes [4] participate in condensation of nucleosomal arrays into 30nm chromatin fiber and there on to higher order structures [5, 3]. Linker histone H1 proteins exist in various isoforms and are organism and tissue specific. The C-terminal domain of H1 determines its binding to the chromatin [6, 8]. The tail interactions organize the chromatin into higher levels of compaction to form 700nm or thicker fibers in the nucleus. The core histone and linker histone terminal regions function independently and additively as revealed from differential centrifugation studies and scanning force microscopy images [8, 6, 7, 10].

Access to DNA requires the disruption of the chromatin assembly which is achieved in vivo by a complex set of histone modifying and chromatin remodeling enzymes. The modifying enzymes modulate the local charge on the nucleosome by modifications of specific residues on the histone tails and hence alter the nucleosome stability and structure. The core and linker histone tails have a high proportion of the basic residues Arginine and Lysine. The covalent modifications that take place on histones include the acetylation of lysines, the methylation of

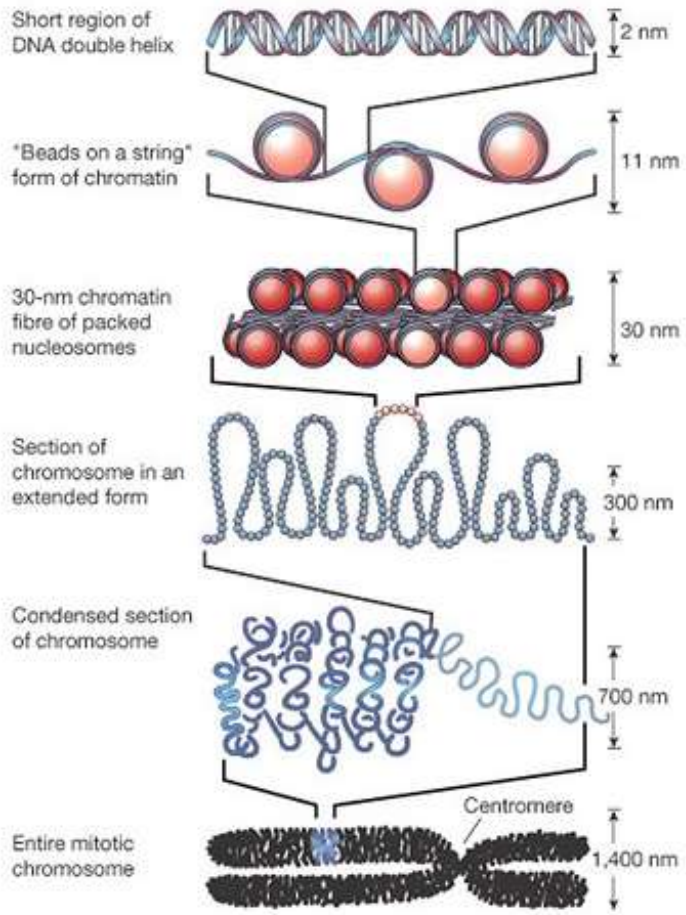

Figure 3.1

Schematic of eukaryotic genome condensation. Figure adapted from, B. Alberts, D. Bray, J. Lewis, M. Raff, K. Roberts, J.D. Watson, *Molecular Biology of the cell*, (Garland, New York, 1994).

lysines and arginines, the phosphorylation of serines and threonines and ubiquitination of lysines [8, 9]. The remodeling enzymes physically reorganize the DNA around the histone octamer in an ATP dependant manner [10, 16, 11, 17, 12, 18]. The specific mechanisms by which the nucleosomes are remodeled are yet to be completely understood [13]. The "loop recapture mechanism" suggests an initial release of a small stretch of DNA at the entry site and the formation of a loop. The movement of the DNA loop around the nucleosome results in nucleosome remodeling. Torsional stresses are also believed to be applied by these enzymes leading to remodeling of the nucleosome. The modifications are required for the binding and activity of "remodeling enzymes". Also, it has been shown that nucleosomes lacking histone N terminal tails are not remodeled by the Drosophila ISWI remodeling complex. However, the removal of N-terminal tails of histones does not affect activity of the yeast SWI/SNF remodeling complex [14].

The histone tail-tail interactions therefore control the structure of chromatin organization and its mechanical properties. Micromechanical experiments on chromatin have led to an estimation of the elasticity of chromatin fibers. In reference [15] a dual-beam optical trap was used to pull on isolated chicken erythrocyte chromatin fibers. The force curves showed that below 20pN the fibers underwent reversible stretching, giving a persistence length of ~30nm and stretch modulus ~5pN/nm for the chromatin fiber. A force >20pN was required to remove the histone proteins from the chromatin fiber. Metaphase chromosomes were shown to be highly extensible when extended even to ~10 times their native length with a Young's modulus of 5±1kPa [16]. Stretching chromatin fiber by micromanipulation and optical tweezer revealed physically distinct populations of disassembly events and a multistage release of DNA [17, reviews 18, 19, 20]. Further micromanipulation of chromatin devoid of the terminal tails of the Histones and chromatin with acetylated histones revealed lower rupture forces [21]. The micromecahnical experiments therefore have demonstrated the role of histone tail-tail interactions and their modifications in the stability of chromatin structure.

Chromatin structure determines the accessibility of the DNA and is considered as a regulatory element for transcription [22]. The modification and remodeling enzymes are recruited specifically to chromatin regions required to be decondensed. Thus, in vivo, regions of condensed and decondensed chromatin states are actively maintained, and

altered when required, by various proteins that tune the local fluidity and hence the accessibility of DNA to proteins. Thus the chromatin architecture over the length scale of clusters of genes determines the local fluidity. In the first part of this chapter we present our studies on changes in the local fluidity due to structural changes of chromatin fibers. In our approach, a micropipette was used to force the rupture of histone tail-tail interactions and histone-DNA interactions and hence disassemble the chromatin fibers isolated from live cells. A phase-sensitive optical trap modulation force spectroscopy technique was developed to probe the local chromatin fluidity as a function of its decompaction. The local fluidity displays an initial increase followed by a reduction upon unfolding the chromatin fiber by mechanical tension. The change in chromatin fluidity was also studied by chemical decondensation of the isolated chromatin fiber, using trypsin. Trypsin digestion of the linker histone tails have been shown to increase the chromatin fiber length in scanning force microscopy images of reconstituted fibers due to decondensation [23]. In our experiments trypsin digestion of histone tails, at a fixed unfolded state, showed enhancement in local fluidity. The subtle changes in the viscoelasticity of chromatin fibers due to rupture of histone tail-tail interactions were hence measurable in our methodology. The rupture of histone tail-tail interactions either by mechanical force or by chemical cleaving of histone tails resulted in changes in the viscoelasticity of chromatin fibers.

The tail interactions are also essential for efficient organization of the genome in cell nuclei. Chromatin condensation achieved by histone tail-tail interactions counter the outward entropic pressure of the fiber and enable packing of chromatin inside the nucleus. The radius of gyration of the chromatin fiber of the human genomic DNA is ~100μm; persistence length of chromatin fiber being ~30nm. The genome is packaged into a nucleus of radius ~20μm; the packing ratio being as high as $\sim 10^4$ in heterochromatin regions and in mitotic chromosomes. The condensation is mediated by histone tail-tail interactions and other non-histone proteins. In the mitotic phase of the cell cycle the chromosome is highly condensed to achieve a size of 1μm due to histone tail-tail interactions as well as other condensation proteins. The chromatin in interphase cells is organized into less dense euchromatin regions and highly condensed heterochromatin regions, rendering the nuclear architecture highly complex as well as

dynamic. The distinct elements that make up the nuclear architecture are the nuclear envelope, made up of nuclear membranes and lamin scaffold, and the chromatin organization [24]. The outer and inner nuclear membranes are separated by a lumenal space and are connected at the nuclear pore complexes. Underlying the nuclear membrane is the lamin network which constitutes the Lamin A and B intermediate filament proteins. The lamin proteins form filaments [25] of persistence length ~100-1000nm. Networks of lamin filaments provide structural scaffolding to the nucleus [26]. The nuclear lamin scaffold has been shown to be highly extensible (25mN/m for Oocyte nuclei [27]). Further, micropipette aspiration experiments on isolated nuclei have shown that the chromatin organization is a load bearing element of the nucleus [28]. The chromatin is known to be anchored to the nuclear lamin scaffold as well as the nuclear membrane [24]. The highly condensed heterochromatin regions are organized along the nuclear periphery and are known to be anchored to the lamin network and the inner nuclear membrane. The chromatin anchorage is mediated by the interactions of HP1 (heterochromatin protein 1) with lamin A in the lamin network and LBR (lamin B receptor) in the nuclear membrane [24] and also by the H2A protein interaction with the lamin proteins [24]. The chromatin organization in a eukaryotic nucleus has therefore a direct bearing on its stability.

In the second part of this chapter the instability of nuclei due to chromatin decondensation by rupture of histone tail-tail interactions is discussed. The decondensation due to trypsin and clostripain digestion in nuclei isolated from HeLa cells led to chromatin swelling and nuclear instability. The chromatin swelling was observed by fluorescence imaging of histone H2B-EGFP fusion protein stably transfected in the HeLa cells. The chromatin swelling was accompanied by expansion of the nuclear lamina and nuclear membrane before the envelope rupture. The stiffness of the nucleus decreased during swelling, as measured using an optically trapped bead adhered to the nucleus. The softening of the nucleus rather than stiffening suggests the softening of the chromatin anchorages to the scaffold, resulting in the scaffold expansion. The pressure on the nuclear envelope due to the chromatin swelling showed an increase by ~3kPa. This was measured by using a cantilever positioned on the nucleus. The increase was followed by a sharp decrease in pressure suggesting sudden breakdown of the nuclear envelope.

3.3 Materials and Methods

3.3.1 Sample Preparation.

Generation of stable lines of HeLa cells expressing H2B-EGFP fusion protein.

HeLa cells, human epithelial cancerous cells, were maintained in culture in an incubator at 37°C with 5% CO_2. The cells were grown in Dulbecco's Modified Eagle Medium (D-MEM, Cat # 11039-021, Gibco, USA), substituted with 5% of Fetal Bovine Serum (FBS, Cat # 16000-044, Gibco, USA) The pBOS plasmid, coding for the H2B-EGFP fusion protein and with the EF1-α promoter was transfected using LIPOFECTAMINE-2000 (Cat#11668-019, Invitrogen, USA). The transfected cells are resistant to the drug Blasticidin. Hence Blasticidin (Catalog #203350-25NG, Calbiochem, USA) was used, at a concentration of 1μg/ml of culture medium, for selection of the transfected cells. The transfected cells were plated in 96 wells, after dilution such that each well had 1 cell. The colonies growing in all the 96 wells were observed over several weeks. A few of these were selected for further expansion based on the uniformity of EGFP fluorescence intensity in all the cells in the colony. The selected colonies were grown in cell culture flasks and the stable cell lines were frozen for future use. The cells in culture were used for the nuclei isolation and chromatin extraction.

Isolation of intact nuclei from HeLa cells expressing H2B-EGFP fusion protein.

HeLa cells, with exogenous H2B-EGFP proteins, were grown to confluence in cell culture flasks, as detailed above. Freshly harvested cells were washed in PBS (pH 7.4) buffer and resuspended in TM2 buffer - 10mM Tris-Hcl pH7.4, 2mM Mgcl2 & 0.5mM PMSF (added fresh prior to use). The cells were incubated for 5` in room temperature and followed by 5` incubation on ice. 0.5% volume/volume of Triton×100 was added and mixed thoroughly before incubating on ice for another 5`. The cells were sheared by passing them through a syringe needle (22 guage) for ~10 times to break the cell membrane. The sample was centrifuged at 0.8rpm for 5min, to isolate the nuclei from

the cell debri. The nuclei were observed under the microscope and Triton-×100 treatment was repeated if the nuclei were found to have cellular debri sticking. Clean isolated nuclei, completely free of cellular debri were used for experiments and all experiments were performed in PBS buffer at pH 7.4.

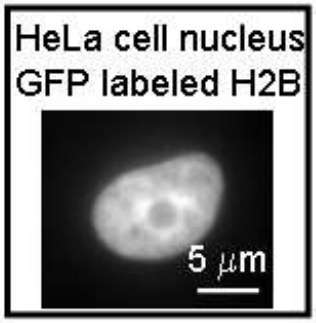

Nucleus isolated from HeLa cells with H2B-EGFP fusion protein.

Chromatin extraction from He-La cells.

For chromatin extraction, the freshly harvested cells were washed with M1 buffer (with 50mM of Tris-cl pH 7.5, 100mM of $Mgcl_2$, 100mM of NH4cl and 4% w/v of PEG3350) and centrifuged (4krpm, 20min). Fresh M1 buffer was added and the cells were mechanically sheared using an insulin syringe (30 gauge needle) to lyse the cell membrane. The sample was centrifuged at 12krpm for 5` to obtain chromatin and nuclei free of cellular debri. The pellet was resuspended in M1 buffer and sonicated for 5` to obtain chromatin pieces of various sizes. The chromatin pieces were sorted out from the remaining debris in a Fluorescence Assisted Cell Sorter (FACS-Vantage, BD), using the (excitation maximum 488nm, emission maximum 520nm) fluorescence of the exogenous H2B-EGFP fusion protein. The chromatin samples were stored at 4°C in PBS buffer (1×, pH 7.4) and used over a week.

Nuclear membrane staining using lipophilic dyes and Hoechst staining of chromatin.

The isolated nuclei were stained with FM4-64 (N-(3triethylammoniumpropyl) -4(6(4(diethylamino) phenyl)hexatrienyl) pyridinium
-dibromide (FM® 4-64), Molecular Probes, Invitrogen, USA) as follows. The nuclei were allowed to stick to poly-D-Lysine coated cover-slips and washed with PBS 7.4

buffer. FM4-64 was added to a final concentration of 0.3µg/ml to a 0.1% solution of BSA (Bovine Albumin fraction-V, RM105 HiMedia Laboratoreis Limited, India) in PBS pH7.4. The above was added to the nuclei and incubated in room temperature for 30 minutes. The free dye in the solution was washed away with PBS buffer (1×, pH7.4) before using the sample for experiments. Hoechst dye staining of chromatin in isolated nuclei was used to observe the DNA after the trypsin decondensation of chromatin.

3.3.2 Phase sensitive measurements in intensity modulated optical trap.

Stiffness of functional chromatin assembly.

Chromatin was isolated from HeLa cells with H2B-EGFP proteins (Materials and Methods). The chromatin pieces were attached to the poly-D-lysine coated glass cover-slip and the cover-slip was mounted onto the PZT stage of the microscope. The micropipette was pulled to a tip size of ~0.5µm using a micropipette puller. The micropipette was coated with poly-D-Lysine by keeping it dipped in poly-D-Lysine solution for ~30` and later dried in the oven at ~100°C for 5`. This was done to ensure firm adhesion of the micropipette to the chromatin. The micropipette was mounted on a motorized XYZ stage (Newport) with a resolution of 50nm. A chromatin piece ~(10-40)µm in size was identified using the H2B-EGFP fluorescence and it was ensured that it was free of debri by fluorescence as well as bright field images. The sample was washed with 50mM NaCl many times and the experiments were performed in 50mM NaCl solution; the chromatin is known to exist mostly as bundles of 30nm fibers at this salt concentration. The chromatin fiber was pulled out using the micropipette, Figure 3.2(a); top panel – bright field image and bottom panel – fluorescence image of H2B-EGFP. The chromatin fiber length could be extended to ~80µm before rupture and was not optically visible. An optically trapped bead of size ~2µm was adhered onto the fiber and the chromatin stiffness was measured using a single axis photodetector (Materials and Methods), Figure 3.2(b).

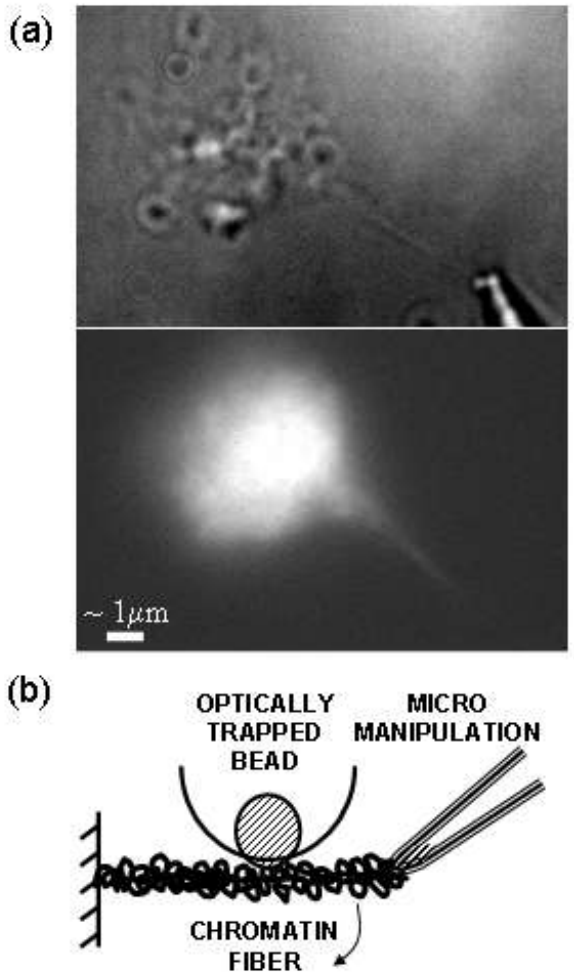

Figure 3.2

(a) Bright field (top panel) and fluorescence images (bottom panel) of chromatin pieces adhered onto the glass cover-slip. The micropipette is used to pull out a bundle of chromatin fibers. Extension of the chromatin fiber leads to decompaction. **(b)** Schematic of the experiment to measure the chromatin stiffness. The optically trapped bead is adhered onto the fiber that is pulled by micromanipulation. The position fluctuation distributions of the trapped bead give the fiber stiffness.

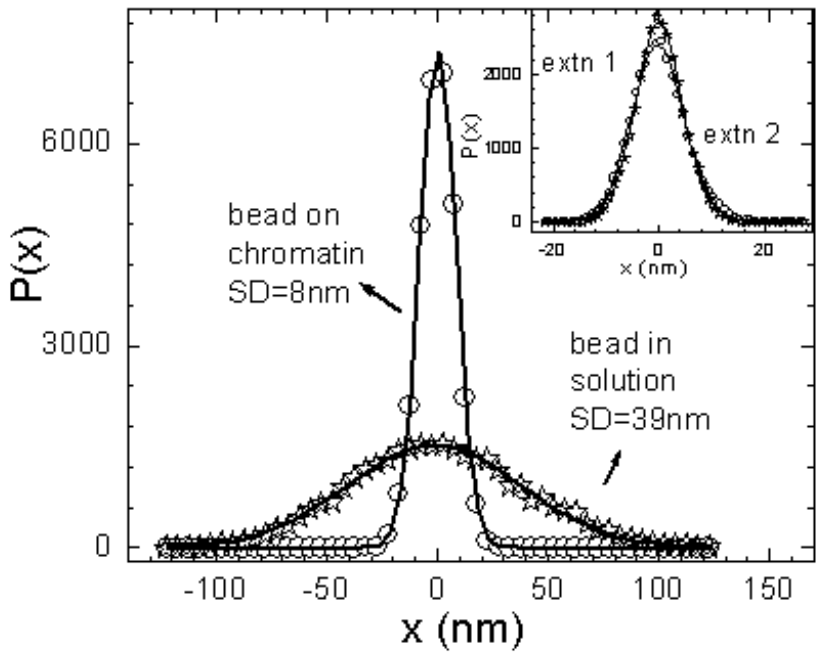

Figure 3.3

Position distributions of the trapped bead in solution (open stars) and the trapped bead adhered onto the chromatin fiber pulled out with the micropipette (open circles). The position time series is acquired at a sampling rate of 5000Hz. The Gaussian fits give the standard deviation values of 39nm for trapped bead in solution (open stars) and 8nm for trapped bead adhered onto the chromatin fiber (open circles). Inset shows position probability distributions of the trapped bead adhered to the chromatin fiber at extensions of ~10μm (open circles) and ~20μm (open stars). The distributions are fit to Gaussian functions and show no variation in the standard deviation values for the above extensions.

The time series of the bead position was obtained at a sampling rate of 2kHz. Figure 3.3 compares the position distributions of the trapped bead in solution and adhered onto the chromatin fiber. The standard deviation of the position histograms was used to calculate the optical trap stiffness and the effective stiffness of the chromatin fiber. The values of the standard deviation are $\sigma_{trap} = 39nm$ for a free bead in solution and $\sigma_{eff} = 8nm$ for the trapped bead adhered onto the fiber under an extension ~5μm. This corresponds to a stiffness value of ~10^{-6}N/m for the optical trap.

The chromatin-trap system is like springs in parallel because the individual stiffness of the springs add up,

$$k_{eff} = k_{trap} + k_{chro}$$

where, k_{eff} is the effective stiffness of the chromatin-trap system, k_{trap} being the trap stiffness and k_{chro} the chromatin stiffness.

Using the relation $\langle \Delta x^2 \rangle = \frac{k_B T}{k_{trap}}$ and $\langle \Delta x^2 \rangle = \sigma^2$ we get the relation for the standard deviations

$$\frac{1}{\sigma_{eff}^2} = \frac{1}{\sigma_{trap}^2} + \frac{1}{\sigma_{chro}^2}.$$

Using $\sigma_{eff} = 8nm$ and $\sigma_{trap} = 39nm$, gives $\sigma_{chro} = 8.2nm$ and a stiffness of $k_{chro} = 0.59 \times 10^{-4}\ N/m$ for the chromatin fiber.

The position distributions were measured for different extensions of the chromatin fiber. The distributions show no change in the standard deviation values for different extensions, as shown in inset to Figure 3.3.

Phase distributions: sensitive probe of local fluidity of chromatin.

We developed a novel methodology sensitive to small changes in viscosity that cannot be measured by the optical trap. In this method the fluctuations in the phase output of the lock-in amplifier is used as a parameter to measure the local solution viscosity and chromatin fluidity. A function generator (Model DS345, Stanford Research Systems, USA) was used to modulate the controller current hence periodically varying the trap potential. The sinusoidal modulation of the laser power (± 20mA) leads to a change in

stiffness of $\pm 2.8 \times 10^{-6}$ N/m. The voltages from the preamplifiers were used as input to the Lock-in amplifier (Model SRS530, Sanford Research Systems, USA), locked to the modulating signal by a TTL synchronous pulse from the function generator. The component of the trapped bead fluctuations at the modulation frequency, measured by the lock-in amplifier gives the response and phase to the periodic potential.

The lock-in amplifier selectively amplifies the desired frequency component of the input signal. A lock-in amplifier is most useful when the signal has many frequency components other than the desired frequency. A reference signal, in-phase with the modulating signal and at the same frequency, is fed into the lock-in amplifier. The Voltage Controlled Oscillator (VCO) of the lock-in amplifier generates two 90° phase shifted signals at the reference frequency and having unit amplitude. These phase shifted signals are multiplied by the input signal, achieved by the "phase sensitive detector-PSD".

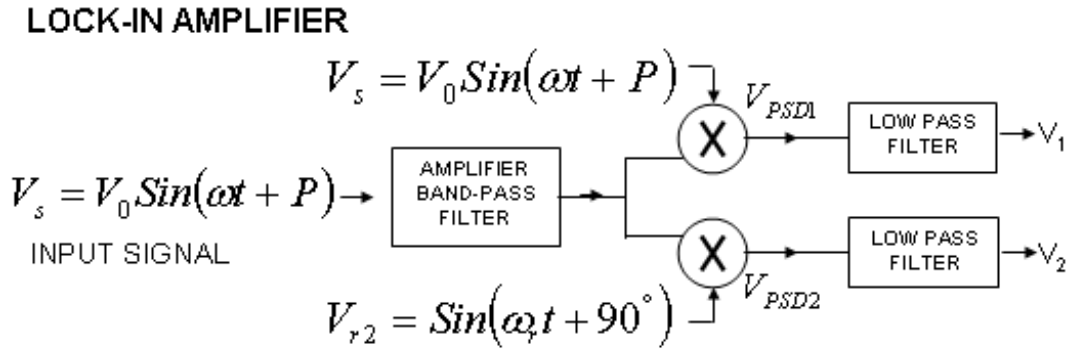

Signal from the experiment

$V_s = V_0 Sin \omega t + P$

where V_0 is the amplitude of the signal, ω is the frequency and P is the phase of the signal with respect to the modulation signal.

The outputs of the VCO are

$$V_{r1} = Sin(\omega_r t)$$

$$V_{r2} = Sin\left(\omega_r t + 90^\circ\right)$$

The PSD multiplies the input signal with the above two reference signals

$$V_{PSD1} = V_0 Sin\left(\omega t + P\right) Sin\left(\omega_r t\right)$$

$$V_{PSD2} = V_0 Sin\left(\omega t + P\right) Sin\left(\omega_r t + 90^\circ\right)$$

$$V_{PSD1} = -\frac{1}{2} V_0 \left[Cos\left(\omega + \omega_r\right) t + P\right] - Cos\left(\omega - \omega_r\right) t + P$$

$$V_{PSD2} = -\frac{1}{2} V_0 \left[Cos\left(\omega + \omega_r\right) t + P\right] - Cos\left(\omega - \omega_r\right) t + P - 90^\circ$$

The above two signals are passed through the Low Pass Filter, which allows only the DC components in the signal. The components of the signal are

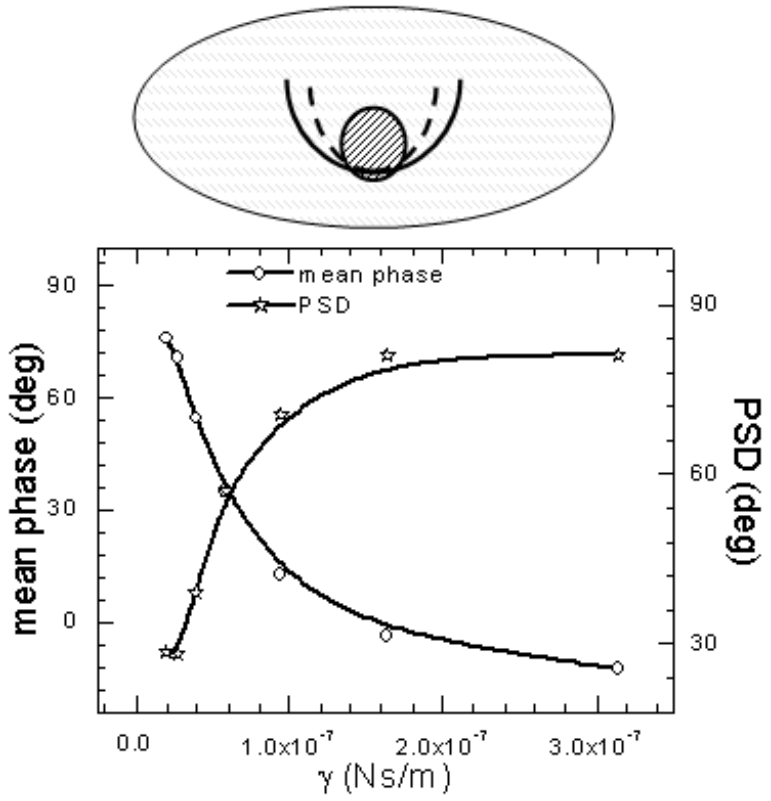

Figure 3.4

Mean phase and the standard deviation phase time series (PSD) of trapped bead plotted for varying solution viscosities. The optical trap stiffness (k_{trap}= 2.6×10^{-6}N/m) is sinusoidally modulated ($k_0=0.8\times10^{-6}$N/m) and the bead fluctuations are measured by using a back-scattered red laser (635nm).

DC only when $\omega=\omega_r$, the signal frequency being the same as the reference frequency. The outputs of the low pass filters are

$$V_1 = \frac{1}{2} V_0 Cos \phi$$

and

$$V_2 = \frac{1}{2} V_0 Sin \phi$$

The desired output voltage is

$$V_0 = \left(V_1^2 + V_2^2 \right)^{1/2}$$

and the phase lag of the experimental output signal with respect to the input modulation signal is

$$P = \tan^{-1}\left(\frac{V_2}{V_1}\right).$$

The mean phase and the standard deviation of the phase time series (PSD) of trapped bead plotted were measured for varying solution viscosities. The bead position fluctuations were measured by using a back-scattered red laser (wavelength 635nm). The back-scattered laser was imaged onto a photodiode partitioned into two halves, to give two voltages proportional to the intensity of the laser on each of the partitions. The above voltages, amplified using low-noise pre-amplifiers were input to the lock-in amplifier, which is frequency locked at the trap modulation frequency (100Hz). The lock-in amplifier gives the amplitude and phase of the bead position at the trap modulation frequency (the time constant of the low pass filter in the lock-in amplifier=300ms). The time-series of the amplitude and phase of the bead fluctuations at the modulation frequency were measured (200 points at acquisition rate of 3Hz; the lock-in time constant being 100ms).

The amplitude output "R" of the lock-in amplifier gives the strength of the bead fluctuations at the modulating frequency. The mean amplitude decreases with increasing solution viscosities, whereas the standard deviation of the R distributions increases, as expected due to greater damping. The mean phase and the standard deviation of the phase histograms of the bead fluctuations are plotted in Figure 5. The standard deviation of phase is ~30^0 for a 2μm diameter polystyrene bead in water (viscosity of 1cp) in a

potential well of stiffness 2.6×10^{-6}N/m, the amplitude of the periodic modulation leading to change in stiffness of $\pm0.8\times10^{-6}$N/m (at 100Hz frequency). The phase standard deviation (PSD) was measured for solutions of varying viscosity, obtained by appropriate glycerol concentration in water. With increase in viscosity to 4.76cp (40% glycerol in water) the spread increases to $\sim70^{0}$, Figure 3.4. With viscosity the damping increases, hence introducing a greater fluctuation of the phase lag of the particle with respect to the periodic driving force. There was no decrease in the trap stiffness with increase in the solution viscosity, as clear in the distributions of position time series of the trapped bead (data not shown). The standard deviation of the distributions should increase with decrease in the trap stiffness. Our data shows that this does not happen (data not shown). Hence though the refractive index of the solution could change at higher glycerol concentrations, it does not affect the trap stiffness in our experiments, since the change in refractive index is negligible.

3.4 Results and Discussions

3.4.1 Measurement of chromatin fluidity.

Tension induced enhancement of chromatin fluidity.

Mechanical tension applied on the chromatin leads to unfolding of the chromatin fiber due to the breaking of the intermolecular bonds, hence modulating the local fluidity. We have studied the local fluidity changes of chromatin bundles when decompacted. We have used a force modulation technique, based on an optical trap, as a local probe of fluidity combined with micromanipulation to mechanically unfold the chromatin assembly.

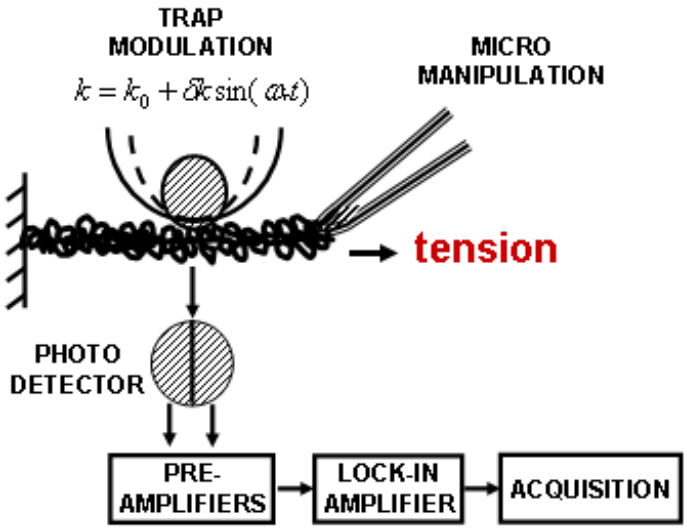

Figure 3.5

Cartoon of the experimental geometry, where the micropipette (tip size ~0.5μm) is used to pull out chromatin fibers from isolated chromatin adhered onto poly-D-lysine coated glass cover-slip. The trap is modulated at a frequency of 100Hz. The optically trapped bead is adhered onto the chromatin fiber non-specifically.

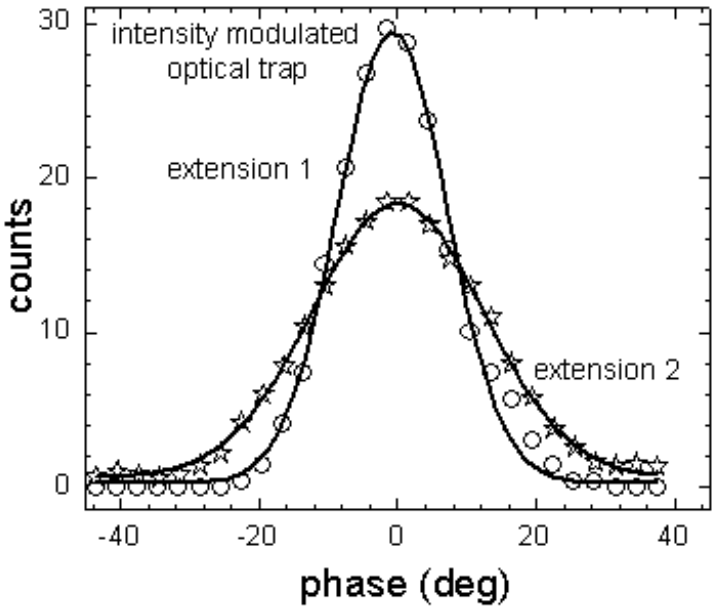

Figure 3.6

Distribution of phase time series of trapped bead adhered onto the chromatin fiber pulled out with the micropipette. The probability distributions are plotted for increasing extensions of the chromatin fiber; ~10μm (open circles) to ~20μm (open stars). The trap stiffness was 2.6×10^{-6}N/m with a change in stiffness of $\pm0.8\times10^{-6}$N/m due to modulation at 100Hz. The lines joining the symbols represent Gaussian fits to the probability distributions giving standard deviations of 16° for 10μm and 25° for 20μm extensions of the chromatin fiber.

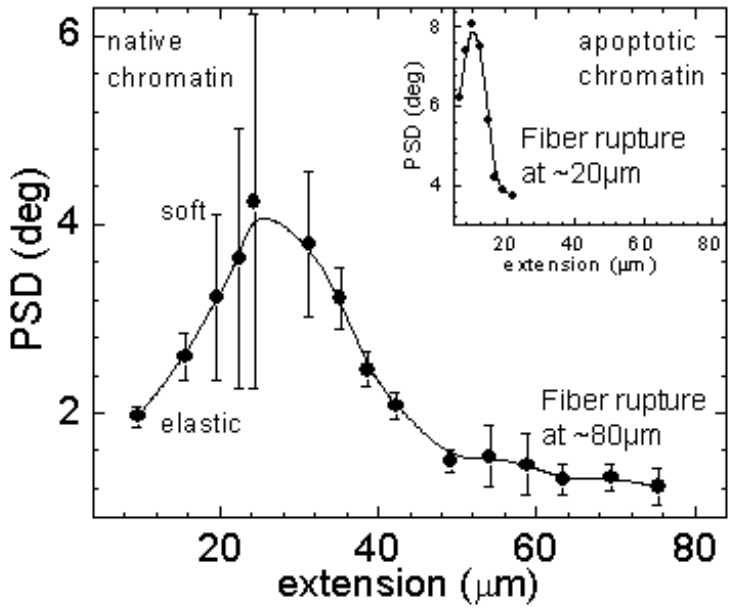

Figure 3.7

Standard deviation of the phase time series of trapped bead adhered onto the chromatin fiber pulled out with the micropipette as a function of increasing extension. The chromatin fiber was extended up to ~80µm beyond which the fiber ruptured. An initial increase was observed in the phase standard deviation calculated from the phase time series of the lock-in output (sampling rate was 3Hz with the lock-in time constant set at 300ms). The line joining the symbols represents spline fit to the data. Inset shows phase standard deviation as a function of extension of chromatin isolated from apoptotic cells. The maximum length the fiber can be extended before rupture is ~20µm. The line joining the symbols represents spline fit to the data.

The trapped bead was adhered onto the pulled out fiber and the response and phase measured as the chromatin was unfolded by mechanical tension, Figure 3.5. The phase distributions show the change in the standard deviation of the phase with increase in applied tension, Figure 3.6. The data points of the histogram are smoothened by adjacent averaging before plotting in Figure 3.6 and the line joining the data points is a spline fit.

With tension the chromatin structure is unfolded due to disruption of the inter-protein interactions in the chromatin, resulting in increase in the relative viscosity and hence the phase width. We observed a characteristic peak in the phase standard deviation, Figure 3.7; an initial increase followed by the values decreasing even below the initial value of $\sim 4^0$. The tether length can be increased to greater than 80μm, the phase width being almost constant for tether length in the range of ~40μm-80μm. At this stage the chromatin fiber is not optically resolved; further increase in tether length results in break in the chromatin fiber.

We observed similar behavior with tension induced decondensation of chromatin isolated from apoptotic cells. The cells were pushed to apoptosis by treating the cells with the drug Staurosporine for ~ 6 hours. Staurosporine is a cell permeable drug that inhibits protein kinases and hence pushing the cells to apoptosis. The chromatin samples from the apoptotic cells were prepared as for the healthy cells. In this case the length to which the fiber could be extruded before fiber rupture was atleast four fold smaller than the length achieved in normal samples (Inset to Figure 3.7). The reduction in the maximum length to which the fiber can be extended, before rupture, could be due to fragmentation of chromatin, which is the hallmark of an apoptotic cell.

In our approach we disrupt the inter-nucleosomal interactions by applying external tension on the chromatin fiber. The mean value of R and its standard deviation change with solution viscosities but are not sensitive to local fluidity changes of chromatin. This is due to the increased stiffness of the chromatin as compared to trap stiffness. The standard deviations of the phase histograms are however were very sensitive to the local chromatin fluidity changes and this was used in our experiments. In our methodology the trap potential shape is modulated rather than the spatial position of the trap. Microspheres in spatially modulated optical traps have been used to measure the viscoelastic properties of polymer gels and other viscoelastic media [29, 33, 30, 34, 31,

35]. The amplitude and phase of the response to the modulation were measured using a lock-in technique. In the above experiments the viscosities measured are homogeneous viscosities assuming no adherence of the microspheres to the viscoelastic media. In our case the chromatin fiber provides a large stiffness (elastic) to the trapped bead compared to the optical trap itself, and the bead is firmly adhered to the chromatin fiber. The relatively small change in the viscosity is therefore not measurable from the position fluctuations alone. Hence we used phase sensitive measurements, where the fluctuation in the phase is the quantity of interest rather than the mean phase itself. The standard deviation of the phase time series obtained gives a measure of the chromatin fluidity. Our results reveal a regime where the nucleosomal arrays are more mobile when the Histone tail interactions are disrupted by tension, Figure 3.8.

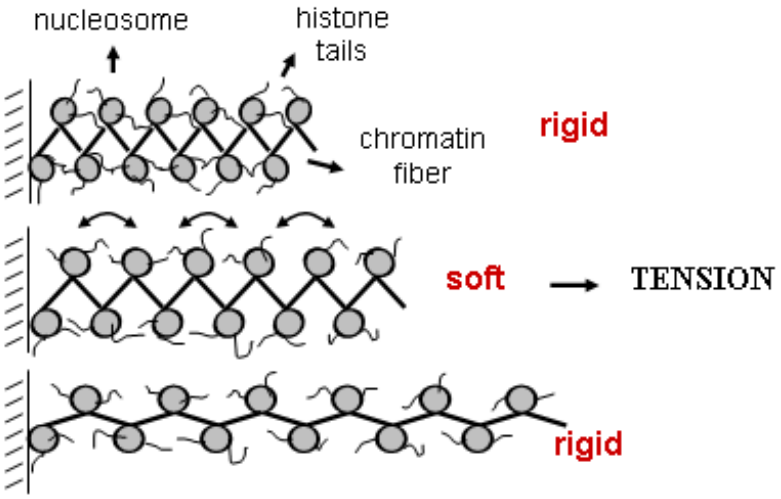

Figure 3.8

The schematic shows the tension induced rupture of the Histone tail interactions leading to decompaction of the chromatin assembly. For a fixed tension, trypsinization of the histone tails results in similar increase in the fluidity of the chromatin.

Trypsin digestion of chromatin leads to enhanced fluidity.

In the previous section inter-nucleosome interactions and hence the chromatin structure was disrupted by mechanical tension. Trypsin is a serine protease which cuts next to the Lysine and Arginine residues of proteins. It initially acts on unstructured terminal domains of protein and later degrades the structured regions. Trypsin digestion of histone tails leads to decondensation of chromatin due to disruption of higher order organization mediated by the protein tails. This is analogous to tension induced decondensation of the chromatin higher order structure. We measured the increase in local fluidity due to trypsin digestion, before the actual breakage of the fibers. The increase in local fluidity of chromatin due to chromatin digestion by trypsin was measured on chromatin fibers pulled out by the micropipette and held at constant length of <10μm, hence fixing the tension. Trypsin was added in the sample well and response and phase time series were measured. The phase histograms were plotted for different time points after addition of trypsin as shown in Figure 3.9. The data points of the histogram are smoothened by adjacent averaging before plotting in Figure 3.9 and the line joining the data points is a spline fit. Decondensation leads to loosening of the fiber, hence increasing phase spread of the trapped bead adhered onto the fiber. The phase width increases to >20° at <10min after adding trypsin as shown in Figure 3.9. Inset to Figure 3.9 shows the step-like jumps (marked by arrows) in the mean position of the bead in the trap which reflects strand breakages due to trypsin. There was a significant increase in the phase standard deviation values due to change in local fluidity before the actual fiber lengthening and strand breakages. This increase in local fluidity is analogous to the elastic - viscous transition observed with tension applied on the chromatin, though in which case the jumps in the mean position of the bead in the trap (marked by arrows in the Figure 3.9) which reflects strand breakages due to trypsin. The results suggest the contribution of inter-nucleosomal tail interactions to chromatin rigidity. During trypsin digestion, eventually the fiber stiffness decreases as the excess DNA gets released as a consequence of decondensation.

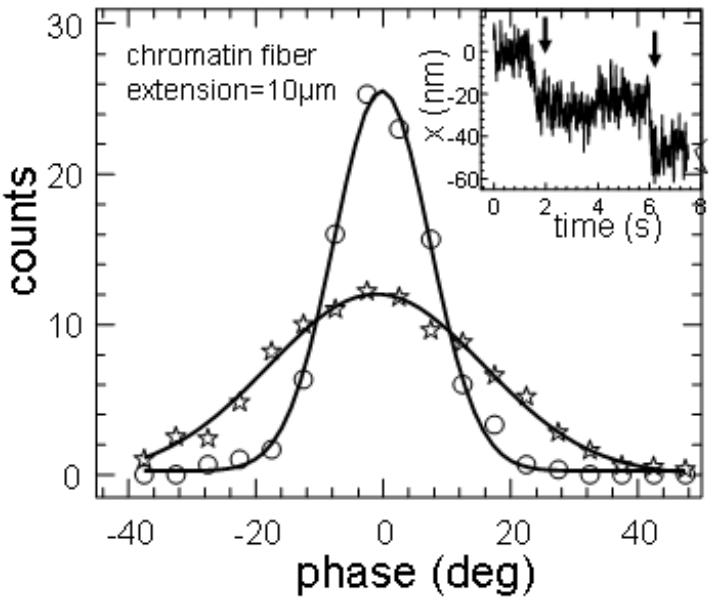

Figure 3.9

Histograms of the phase time series of a bead adhered onto the chromatin fiber being digested with trypsin. A bundle of chromatin fiber is pulled out to a length ~10μm using the micropipette and an optically trapped bead is adhered onto it, trap stiffness being 2.6×10^{-6}N/m with change in stiffness of $\pm 0.8 \times 10^{-6}$N/m due to modulation at 100Hz. The figure compares the histograms before trypsin digestion and at ~10min after trypsin addition in the sample well. At later time points the chromatin fiber relaxes indicating an increase in length and is eventually ruptured. The lines joining the symbols represent Gaussian fits to the distributions, the standard deviations of the distribution being 16.5° and 7.5° for the two time points. Inset shows a typical position time series of the bead adhered to the chromatin, held at a constant length of ~10μm and trypsin digested. There are sudden jumps in the bead position, indicating strand breakages.

3.4.2 Balancing chromatin assembly within the cell nucleus.

Decondensation of the chromatin structure in isolated nucleus, was achieved by trypsin digestion of histone tails of the chromatin. The isolated nuclei were adhered to poly-D-lysine coated glass cover-slips and the sample was washed with 1ml of PBS pH7.4 buffer to remove all the PMSF in the TM2 buffer. PMSF would inhibit the protease action of trypsin in the nuclei. The trypsin (at appropriate concentrations) was added to the sample well and the nuclear swelling was observed on a confocal fluorescence microscope.

Fluorescence confocal images were taken on Zeiss Confocar Laser Scanning Microscope, using the 488nm line of Argon-Ion Laser and 543nm of He-Ne Laser. A 63×, 1.4 Numerical Aperture Oil immersion objective was used for all the images. The confocal z-slices of the nucleus were taken using a pin-hole of 200μm. The pin-hole size was maintained to ensure collection from a volume of ~1μm at the object plane. The system was used in the multi-track mode, which prevents leakage between channels, to image the chromatin using H2B-EGFP fluorescence (excitation wavelength 488nm, emission wavelength 520nm), the lamin scaffold using the Lamin-EFGP fluorescence (excitation maximum 488nm, emission maximum 520nm) and the membrane using the FM4-64 fluorescence (excitation maximum 515nm, emission maximum 640nm). Scanning of the laser beam in the object plane is achieved by moving the mirror reflecting the laser into the microscope. The emission light is passed through the appropriate filter to select the wavelength of interest and detected on a PMT. A multi-photon excitation (maximum 750nm) was used to image the Hoechst (excitation maximum 346nm, emission maximum 460nm) staining of the DNA in the nucleus.

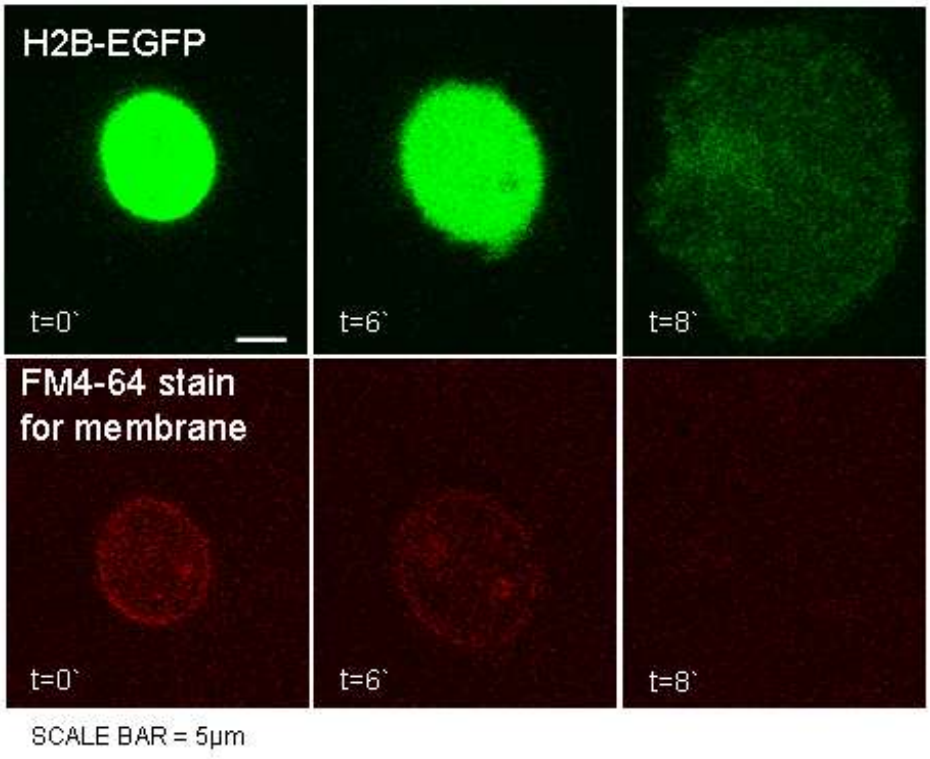

Figure 3.10

Confocal fluorescence images of nuclei with H2B-EGFP fusion protein: excitation maximum 488nm, emission maximum 512nm (top panel) and with membrane dye, FM4-64: excitation maximum 515nm, emission maximum 620nm (bottom panel). The confocal z-stacks were taken on Zeiss Confocal microscope with 63×, 1.4NA oil immersion objective and the z-slice with the largest area of the nucleus were selected from each stack. The top row of the figure shows such slices at time points of 0`, 6` and 8` after adding trypsin indicating increase in the nuclear membrane surface area. At further time points the membrane is ruptured as shown by disappearance of the fluorescence from the membrane (images not shown). Scale bar for all images is 5µm.

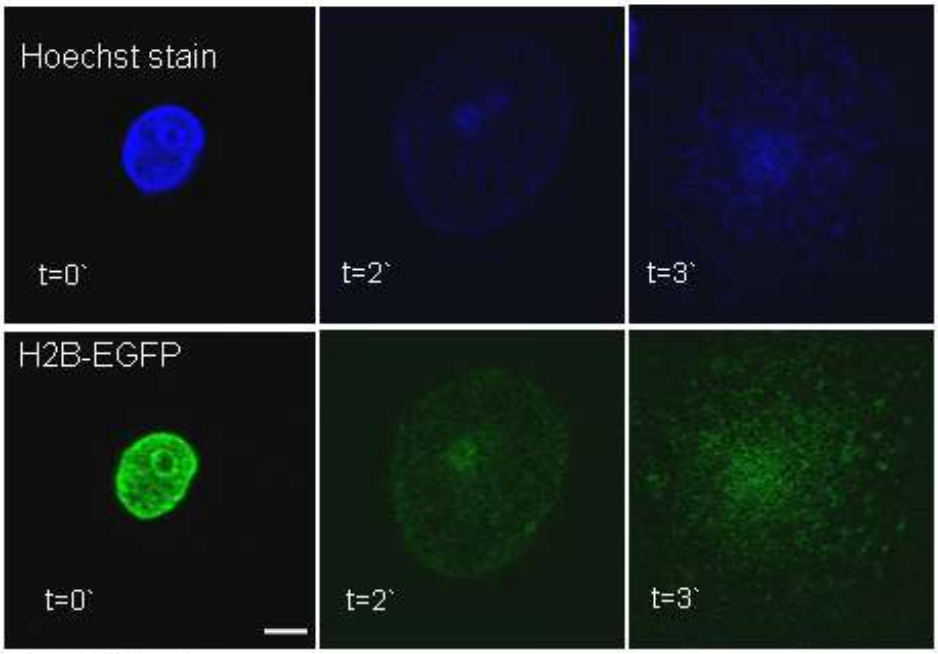

Figure 3.11

Confocal fluorescence images of nuclei with Hoechst dye staining of DNA: excitation maximum 346nm, emission maximum 460nm (top panel) and H2B-EGFP fusion protein: excitation maximum 488nm, emission maximum 520nm (bottom panel). The confocal z-stacks were taken on Zeiss Confocal microscope with 63×, 1.4NA oil immersion objective and the z-slice with the largest area of the nucleus were selected from each stack. The figure shows such slices at time points of 0`, 2` and 3` after adding trypsin indicating swelling of DNA due to decondensation. Scale bar for all images is 5µm.

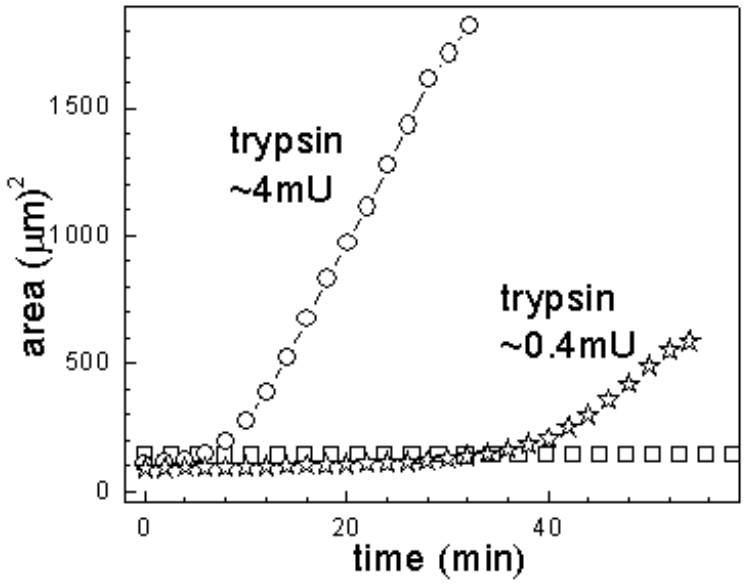

Figure 3.12

Area of the nucleus obtained from confocal images, taken as described before, as a function of time. The plots show the increase in area obtained from confocal images with trypsin digestion (open circles, ~4mUnits of trypsin and open stars, ~0.4mUnits of trypsin). Open squares show that the area remains constant with trypsin digestion when the nuclei are Glutraaldehyde fixed (glutraaldehyde concentration of 1%, for ~15`).

The nuclear swelling due to the trypsin decondensation of chromatin in isolated nuclei is shown in Figure 3.10. The top panel shows the H2B-EGFP fluorescence images and the bottom panel shows the membrane stain images of trypsin digested nuclei. The time lapse images of the nucleus show that the Histone (H2B-EGFP) proteins are not cleaved by trypsin over our experimental time scales. There is an initial increase in the membrane area before membrane ruptures. Images of Hoesct dye staining of DNA, top panel in Figure 3.11, show that the DNA is intact after trypsinization and is decondensed. In Figure 3.12 we plot the increase in area of the nucleus obtained from the chromatin images (H2B-EGFP) for trypsin digestion at concentrations of ~4mUnits (open circles) and ~0.4mUnits (open stars) in 100µl of sample volume. At 4mUnits trypsin concentration the area of the isolated nucleus increases by ~4 fold in less than 1000s, suggesting a volume increase of at least 8 times.

Rupture of the protein interactions responsible for chromatin compaction due to trypsin results in the entropic expansion of the decompacted chromatin. The 30nm fiber is organized by the arrangement of ~10 mononucleosomes (2400bp of DNA) along a fiber length of ~10nm, each mononucleosome constituting ~240bp length of DNA. This corresponds to 816nm of DNA in a stretch of 10nm of the chromatin fiber. For the complete genome length of ~1m the 30nm chromatin fiber length would be 0.012m. The persistence length of the chromatin fiber being 30nm the random coil size of the total genome would be ~100µm. The initial radius of the isolated nucleus is atleast one fifth the radius of the random coil, suggesting further compaction of the 30nm fiber. The pressure of entropic expansion of the decompacted chromatin results in nuclear expansion. To validate the conclusion that chromatin decondensation and the resulting entropic expansion are directly responsible for the nuclear swelling, we used chromatin pieces isolated out of the nuclei. The chromatin pieces were obtained by rupturing the above nuclei by sonication and purifying the chromatin from the cellular debris by FACS (refer to Materials and Methods). Trypsin induced swelling was also observed on chromatin pieces isolated from the nuclei. This suggests that the nuclear swelling primarily arises due to chromatin decondensation and the chromatin is at least one of the major factors contributing to the nuclear architecture.

Lamin network disruption due to chromatin decondensation and swelling.

The nuclear swelling induced by trypsin digestion, could be due to a combinatorial effect of many factors; chromatin decompaction induced breakages in chromatin anchoring to the lamin scaffold and disruption of the lamin scaffold itself, being major contributors. The anchorage of the chromatin to the envelope is achieved by the interaction of DNA and the histone proteins with various nuclear envelope proteins. The nuclear envelope consists of the inner nuclear membrane (INM), the outer nuclear membrane (ONM) and the lamin scaffold [32]. The lamin scaffold is made of the lamin A and B intermediate filament proteins. The lamin proteins belong to the type V of the intermediate filament proteins, the persistence of intermediate filaments being in the range ~100-1000nm. [33]. There are two major types of laminA proteins – LaminA and LaminC; and two types of Lamin B proteins – LaminB1 and LaminB2. The lamin monomer has a central α–helical rod domain flanked by N and C terminal head and tail domains [34]. Two parallel helices form a two stranded coiled-coil structure, with the two globular domains consisting of the tails at one end, and the heads domains at the other. The two globules are absent in tail-less lamin mutants but are retained in headless lamin mutants. These lamin dimers of length ~52nm form polar filaments. The radius of the filament formed *invitro* has been measured to be ~10nm by electron microscopy [34]. Rheology experiments on *invitro* reconstituted Lamin networks showed strain-hardening, with the network stiffening under stress [35]. The above experiments also show that the lamin network can undergo large deformations before breakdown.

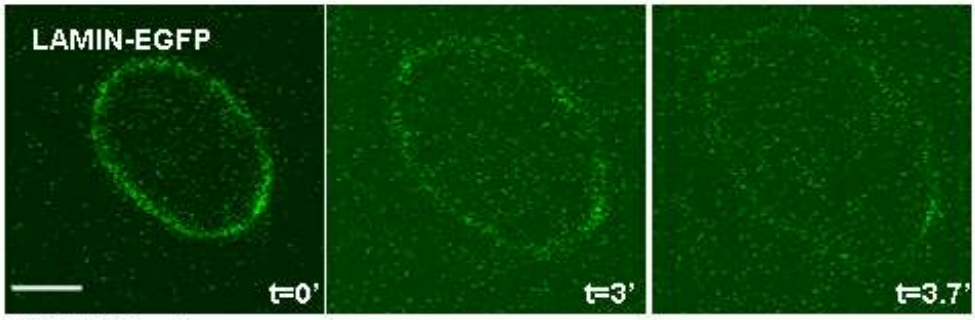

Figure 3.13

The time lapse fluorescence images show the increase in the size of the lamin network when digested with trypsin. The images were taken using the fluorescence of the lamin-EGFP fusion protein. The scale bars indicate 5µm and the time "t" is in minutes.

We studied the lamin reorganization and rupture independently during chromatin decondensation. The HeLa nuclei with the LaminB protein fused with EGFP protein were used for fluorescence imaging of the lamin scaffold. The nuclei were isolated from the HeLa cells that were transfected with the lamin-EFGP plasmid. The images in Figure 3.13 show the increase in the circumference of the lamin scaffold due to digestion of the nuclei with trypsin. The circumference of the lamin network shows an increase due to the chromatin decondensation. The increase in the lamin circumference is followed by a sudden rupture of the scaffold. The results suggest that the decondensing chromatin could release the tension on the scaffold at chromatin-envelope anchorage points leading to scaffold expansion. Also the lamin network, known to be extensible, would expand under the entropic pressure of decondensing chromatin. These observations show that the lamin network extension is controlled by the state of chromatin condensation.

Chromatin swelling due to specific digestion of Histone tails.

Trypsin protease specifically targets the unstructured terminal regions of proteins and is not limited to histone proteins. We therefore also used clostripain (Sigma) which specifically targets the terminal regions of the histone proteins [36]. The nuclear swelling due to clostripain digestion was followed in nuclei with the H2B-EGFP proteins as well as in nuclei with the lamin-EGFP proteins. The clostripain (concentration of 4mUnit in 100µl of sample volume) was activated using DTT (2.5mM) and calcium acetate (1mM), for ~20min in room temperature prior to addition into the sample. Figure 3.14 (top panel) shows the H2B-EGFP fluorescence images of the clostripain treated nuclei. The nuclei showed swelling and rupture similar to that digested with trypsin. In Figure 3.15 the increase in the area of the nucleus, obtained from the H2B-EGFP images is plotted. There was ~5 fold increase in the area due to clostripain digestion of the histone tails. The bottom panel of Figure 3.14 shows the lamin network expansion due to the

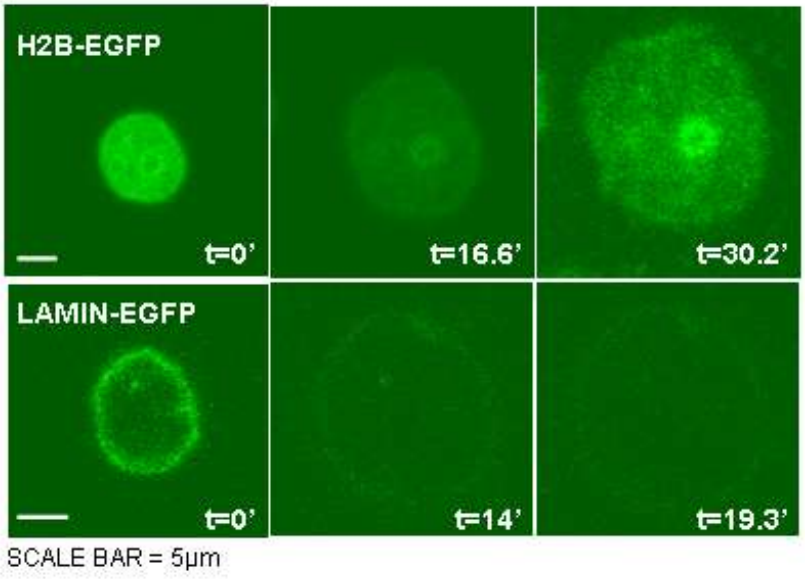

Figure 3.14

The time lapse fluorescence images show isolated nuclei with H2B-EGFP fusion proteins: excitation maximum 488nm, emission maximum 520nm, when digested with clostripain (concentration of 4mUnit in 100µl of sample volume). The clostripain was activated using DTT (2.5mM) and calcium acetate (1mM) for ~20min prior to using it in the experiment. The top panel in the figure shows images of H2B-EGFP and the bottom panel of the lamin-EGFP fluorescence in the nuclei. The scale bars represent 5µm and the time "t" is in minutes.

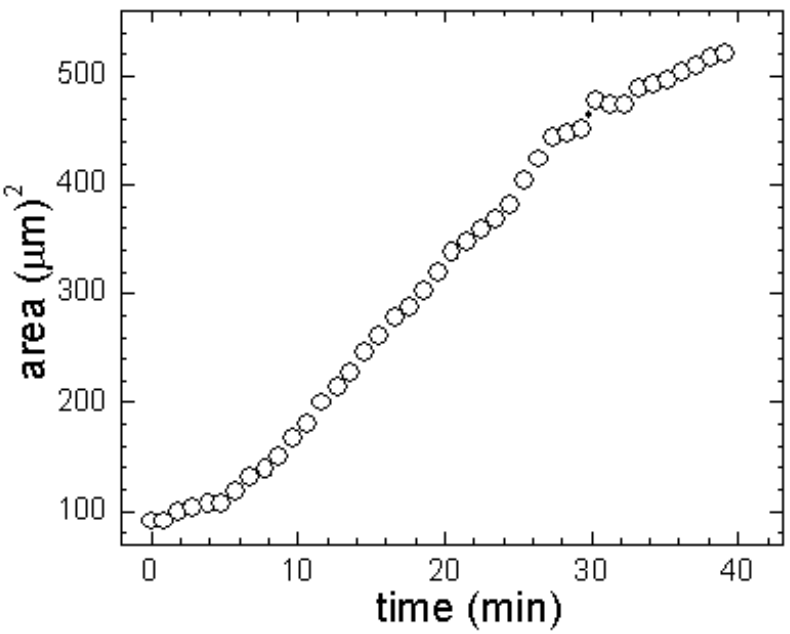

Figure 3.15

The increase in the area as a function of time during clostripain digestion of the nuclei. The values of the area are obtained from the H2B-EGFP images shown in figure 3.14.

chromatin swelling. The lamin network expansion is apparent before it ruptures. These results indicate that the lamin scaffold is held under tension by the chromatin. The scaffold expands due to the tension released during the decondensation of the chromatin. Subsequent decondensation and entropic expansion of the chromatin causes the disruption of the lamin scaffold.

Pressure generated during nuclear swelling using AFM cantilever.

The pressure on the nuclear membrane, due to decondensation of higher order chromatin structure by trypsin digestion leads to initial increase in membrane area and expansion of the lamin scaffold. In order to estimate the magnitude of the pressure, we directly measured the force during the swelling using an Atomic Force Microscope cantilever. A soft cantilever (stiffness=k_{cant}=0.02N/m, Park Scientific, USA) was positioned on the nucleus stuck on poly-D-Lysine coated cover-slip, as shown in the experimental schematic in Figure 3.16. The cantilever of length 200μm and width 20μm (MLCT - Microlever Probes, Rectangular-B, Veeco Metrology group, USA), was mounted on a WITEC Alpha-SNOM microscope. The deflection of the cantilever was measured by using an Infrared laser (920nm) which is incident on the cantilever and the reflected light imaged onto a quadrant photodetector. A change in voltage of 1V in the photodetector amplifier output corresponds to a cantilever deflection of 0.223μm, as calibrated against a hard surface (cover-slip). This calibration was used to calculate the force on the cantilever, using the stiffness value of 0.02N/m for the cantilever, as specified by the company. It is ensured that the experiment is performed in the linear regime of the cantilever response and the detector response.

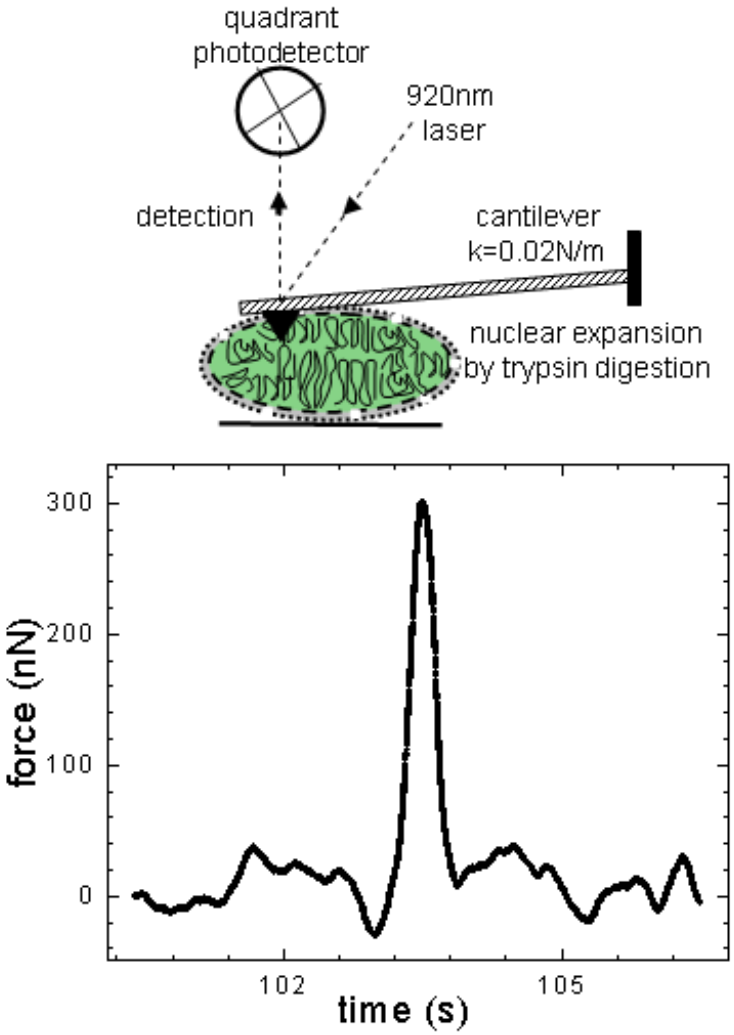

Figure 3.16

Estimation of pressure on the membrane due to chromatin decompaction using a cantilever; experimental schematic is shown in the figure. The force due to nuclear swelling was calculated assuming a linear spring approximation for the cantilever. A maximum force ~200nN was measured for nuclear swelling due to trypsin digestion after which the force falls to the initial value due to complete rupture of the nucleus. A high concentration (~100mUnits) of trypsin was used to minimize the time of the swelling in order to avoid long time scale mechanical drifts.

The deflection due to nuclear expansion was measured as a function of time after trypsin addition; high trypsin concentration was used to reduce the time of measurement and hence the mechanical drifts which are unavoidable. The force on the cantilever was obtained by using $F = k_{cant} x$, where "k_{cant}" is the cantilever stiffness (linear spring for small deflections) and "x" is the cantilever deflection. The pressure as a function of time is plotted in Figure 3.16 showing an increase of ~3kPa, before the nucleus disintegrates beyond which the cantilever deflects back to its initial position. The chromatin swelling results in a surprisingly high force on the membrane prior to rupture. The pressure on the membrane prior to rupture is ~3kPa, corresponding to a force of 200nN over an area of contact of 100μm^2 between the nucleus and the cantilever. Since the nucleus is covered by the cantilever, the pressure was calculated using the area of cross-section of the nucleus (100μm^2). The chromatin swelling results in a surprisingly high force on the membrane prior to rupture. The work done on the cantilever by the entropic forces that cause the chromatin swelling was measured to be ~$10^8 k_B T$. This sets a lower limit to the internal energy stored in the nucleus as a result of chromatin compaction. The sharp relaxation of the cantilever back to its undeflected position suggests a sudden breakdown of the nuclear envelope due to chromatin swelling.

Excess membrane area available for nuclear expansion.

The pressure of the chromatin entropic expansion is also accompanied by an increase in membrane surface area as evident from the confocal images. If the swelling was not accompanied by increase in the membrane area, released probably from excess membrane accumulated in folds, one would expect an increase in membrane tension and bursting of the membrane without allowing swelling of the nuclear membrane. But the fluorescence images show that there is a definite increase in membrane area accompanying the increase in nuclear size. The confocal images of nuclear membrane showed an increase in the surface area of membrane by at least 2 fold before rupture Figure 3.10. A two fold increase in the projected area of the nucleus would imply a similar increase in the total surface area. Earlier reports show similar swelling of isolated nuclei due to reduction in salt concentration [28], where in addition to swelling of nuclear membrane smoothening of the lamin network is also observed, both of which are

reversible. There is therefore a large excess of membrane area available for the nuclear swelling, without requiring the actual stretching of nuclear membrane and consequently rupture. The results show that the excess membrane area is released. This is a direct consequence of chromatin swelling and probably also due to disruption of other protein structures or scaffolds in the nucleus and the disruption of chromatin anchorages to these structures.

Softening of the cell nuclei during nuclear swelling using an optical trap.

The change in stiffness of the nucleus during chromatin decondensation was probed directly using an optical trap. The position fluctuations of an optically trapped bead positioned on the nuclear membrane was monitored during trypsin digestion of the chromatin. A 2µm diameter sized bead was nonspecifically adhered onto the nuclear membrane and confined to the center of the optical trap, as shown in Figure 3.17(a). The position fluctuations of the bead were measured, by imaging the red laser back-scattered from the trapped bead onto a photodiode (Materials and Methods). The change in the position fluctuation distributions of the bead is a direct measure of the change in the stiffness of the isolated nuclei, Figure 3.17(b). Figure 3.17(c) shows the increase in the bead fluctuations with time, due to trypsin digestion (concentration ~4mUnits in 100µl sample volume). The standard deviation increases from $\sigma_{eff}^2 \sim 10nm$ to $\sigma_{eff}^2 \sim 30nm$, the standard deviation for a trapped bead in solution being ~50nm. Increase in the bead fluctuations reflects the nuclear softening due to protein digestion in the nucleus. Considering the trap-nucleus system as springs in parallel the effective stiffness k_{eff} given by $k_{eff} = k_{nuc} + k_{trap}$, where k_{nuc} is the stiffness of the nucleus and k_{trap} is the trap stiffness.

Using $\left\langle \Delta x_{eff}^2 \right\rangle = \frac{k_B T}{k_{eff}}$ and $\left\langle \Delta x_{eff}^2 \right\rangle = \sigma_{eff}^2$ for the effective stiffness

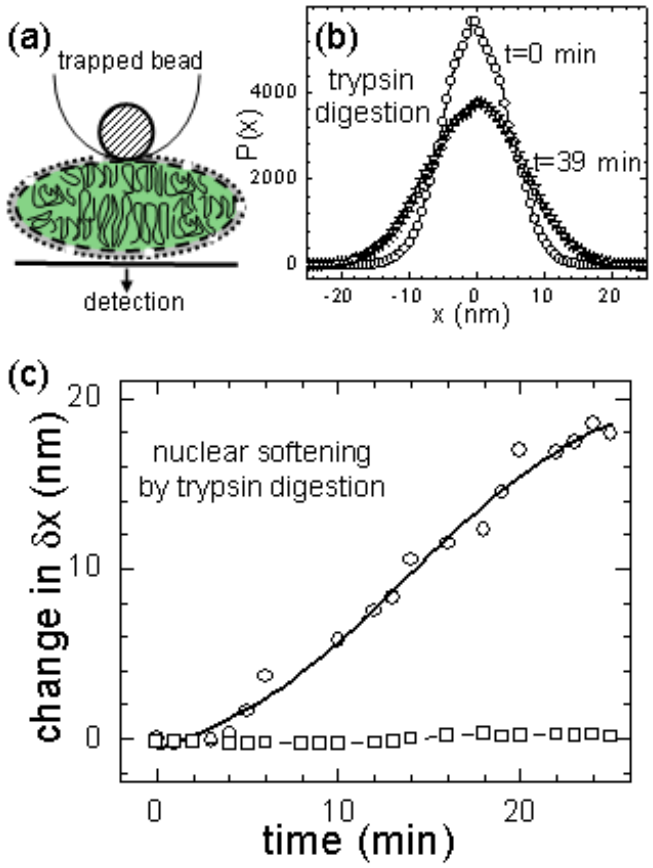

Figure 3.17

(a) Softening of nucleus measured using an optically trapped bead adhered on the nucleus stuck to poly-D-Lysine coated cover-slip as shown in the experimental cartoon. **(b)** The position histograms of the bead fluctuations about the trap centre. **(c)** Plot of the width of these distributions as a function of time, trypsin (closed circles) and Glutaraldehyde fixed nuclei; 1%, 15' (open squares). The trap stiffness in all cases was ~10^{-5}N/m and the position time series were acquired at a sampling rate of 5000Hz. The width for a bead trapped in solution is ~100nm.

and similarly for k_{trap} and k_{nuc} we obtained the nuclear stiffness change during swelling. The nuclear stiffness changed from $k_{nuc}=3.84\times10^{-5}$N/m to $k_{nuc}=2.84\times10^{-6}$N/m. Hence, nuclear swelling is not accompanied by stiffening of the membrane, rather the nucleus is softened. As a control nuclei fixed with Glutaraldehyde were treated with trypsin, and as shown in Figure 3.17(c), the standard deviations of the position histograms do not vary with time with the same trypsin concentration as in the unfixed case.

The results show that the chromatin organization determines the nuclear stiffness; chromatin decondensation and its softening leads to the nuclear softening. These observations suggest the softening of the chromatin anchorages to the nuclear envelope leading to the nuclear softening. Experiments on isolated TC7 epithelium cells showed that the aspiration of the nuclei resulted in buckling of Lamin external to the aspirated regions [28]. This suggests that the tension is coupled to Lamin through distinct internal foci provided by the chromatin. Further, local decompaction and softening is essential for accessibility of DNA during transcription and other DNA based activities. As was described in the first part of this chapter, with rupture histone tail-tail interactions such local softening can be achieved. In trypsinized nuclei, chromatin decondensation and softening of the chromatin anchorages leads global softening of the nucleus.

Anisotropy imaging of the chromatin during nuclear swelling.

The decondensation of the chromatin during trypsin digestion was followed by Anisotropy images of the nucleus taken using the H2B-EGFP fluorescence. We measured the changes in rotational mobility of the histone H2B-EGFP during chromatin decondensation due to trypsin digestion by anisotropy imaging.

Fluorescence anisotropy gives the rotational mobility of the fluorescent molecules. When the fluorescent molecule is excited with a polarized laser, the emission polarization will be parallel to the excitation polarization if the molecule has not changed its orientation in the time between excitation and emission, which

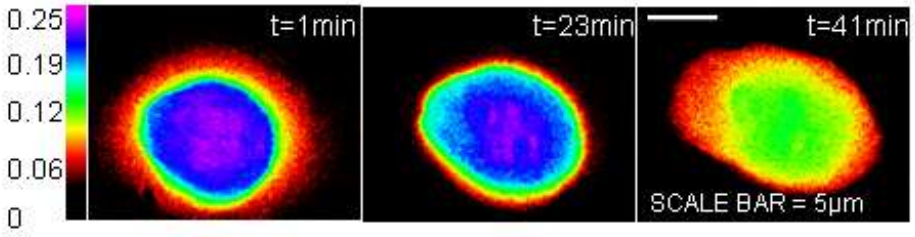

Figure 3.18

Anisotropy images of trypsin induced decondensation of chromatin in isolated nucleus. The color code representation of the anisotropy values is also shown in the figure.

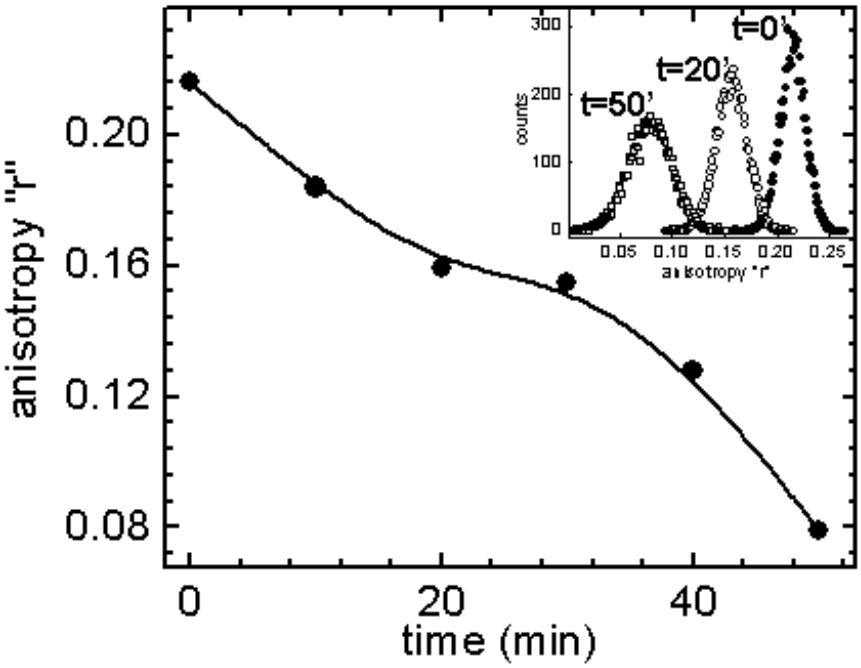

Figure 3.19

Change in the mean value of anisotropy obtained from the images shown in Figure 3.18. The mean value of anisotropy change from ~0.22 to 0.07. Anisotropy distributions during trypsin digestion at time points 0', 20' and 50' are shown in the inset to the figure.

is of the order of “nanoseconds”. The change in the polarization of the fluorescence emission therefore gives the rotational mobility of the molecule. The fluorescent molecule EGFP in our case is fused to the core histone protein H2B. Hence the anisotropy depends on the rotational mobility of the H2B protein in the chromatin structure. Two analyzers with their polarization axes parallel and perpendicular respectively are alternatively placed in the emission path. Hence the camera is either exposed to the component of the emission fluorescence parallel or alternatively the component perpendicular to the excitation polarization. An inverted microscope (model IX71, Olympus, Japan) with a high numerical aperture objective (100× magnification and 1.4 numerical aperture) was used for the anisotropy imaging. An intensified charge coupled camera (Cascade 650; Roper Scientific, USA) was used for imaging. The camera consisted of 653×492 pixels each of size $(7.4\mu m)^2$.

The parallel and perpendicular images were analysed to obtain the anisotropy image using LabView programming (version 5.1; National Intruments, USA).
Anisotropy is given by

$$a = \frac{I_{\text{II}} - I_{\perp}}{I_{\text{II}} + 2GI_{\perp}}$$

where, I_{II} is the parallel image, $I_{\perp}$ is the perpendicular image and G is the G-factor of the experimental setup. The G factor is estimated by measuring the ratio of the parallel to the perpendicular intensities for Fluorescein isothiocyanate (FITC) and comparing it the expected ratio of 1. The expected ratio is 1 since FITC is a very small molecule and it rotational mobility timescales is very short compared to the time scale of emission.

The anisotropy images at different time points during the trypsin digestion are shown in Figure 3.18. The color code representation of the anisotropy values is also shown in the figure. The histograms of the anisotropy for each image were plotted from the anisotropy values at each pixel of the images. The distributions of the anisotropy at different time points is shown in inset to Figure 3.19. The mean value of the anisotropy decreased with trypsin digestion from 0.22 to 0.07, as shown in Figure 3.19. Trypsin decondenses the higher order structures hence leading to changes in anisotropy values. The initial values of anisotropy vary over different nuclei. The standard deviation of the anisotropy distribution for each image increased with time of digestion as shown in the

distribution in inset to Figure 3.18. The fluorescence intensity decreased with decompaction of DNA by trypsin. The mean anisotropy changes and the anisotropy images validate the decondensation of chromatin in isolated nuclei due to trypsin digestion.

3.5 Conclusions

A new method has been developed to detect subtle viscoelastic changes due to structural variations of soft biological samples. The phase sensitive methodology applied is non-invasive and can measure local viscoelastic changes. This methodology maybe applied to measure small variations in chromatin fluidity resulting from biologically relevant chromatin based processes, like chromatin remodeling.

Our results show that the chromatin assembly determines the local fluidity. We found an increased fluidity due to chromatin decompaction by tension before the fluidity decreased for further decompaction. Decompaction in our experiments was achieved by tension induced rupture of the histone protein tail interactions or by trypsin digestion of the histone tails.

The histone tail interactions are responsible for the compaction of the 30nm chromatin fiber, that has a radius of gyration ~70µm, into a nucleus of size ~10-20µm in diameter. The nuclear envelope is hence held under tension due to the chromatin anchorages to the envelope. In live cells this inward tension is compensated by the cytoskeletal filaments maintaining the nuclear size. We show from our experiments that the chromatin provides the major component contributing to the stiffness of the nucleus. Decompaction resulted in local softening of the nucleus as measured by the increased fluctuations of the trapped bead adhered onto the nucleus (Figure 3.17). There was an order of magnitude change in the nuclear stiffness from $k_{nuc}=3.84\times10^{-5}$N/m to $k_{nuc}=2.84\times10^{-6}$N/m, due to trypsin induced nuclear swelling.

Trypsin digestion induced decondensation of the chromatin, leads to chromatin entropic expansion and nuclear swelling and rupture, Figure 3.20. The lamin images showed an initial expansion of lamin network before its rupture. This suggests that the chromatin condensation in the nucleus results in a tension on the lamin scaffold. Our results also show that lamin can under large deformations before breakdown. Decondensation of the chromatin leads its

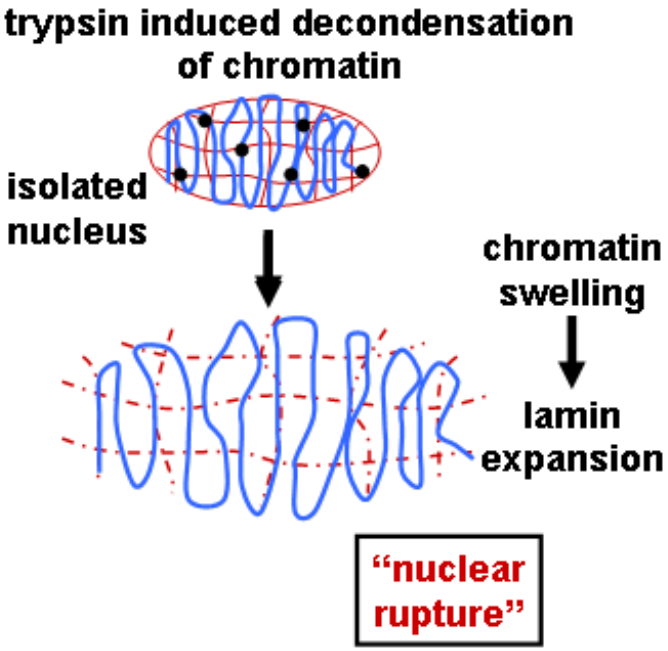

Figure 3.20

Schematic of trypsin digestion of chromatin in isolated nuclei. Decondensation leads to entropic expansion of chromatin and hence nuclear swelling followed by rupture. Chromatin is indicated by blue lines in the figure and lamin by the red lines. There is an initial lamin expansion due to the decondensation of chromatin and subsequent release of tension. Further expansion of chromatin leads rupture of the lamin scaffold and the nuclear membranes.

entropic expansion initially pushing the envelope out and eventually rupturing it. The rupture was observed to be sudden and cooperative across the surface of the nucleus. The scaffold expansion and rupture therefore suggest the role of the chromatin anchorage in the nuclear envelope stability.

3.6 References

1. Olins D. E. and Olins A. L. *Nat. Rev. Mol. Cell. Biol.* **4**, 809 (2003).

2. Luger K., Mader A. W., Richmond R. K., Sargent D. F. and Richmond T. J. *Nature.* **18**, 251 (1997).

3. Allan J., Rau D. C., Harborne N. and Gould H. *J. Cell. Biol.* **98**, 1320 (1984).

4. Allan J., Hartman P. G., Crane-Robinson C. and Aviles F. X. *Nature.* **288**, 675 (1980).

5. Zheng C. and Hayes J. J. *Biopolymers.* **68**, 539 (2003).

6. Hendzel M. J., Lever M. A., Crawford E. and Th'ng J. P. *J Biol Chem.* **279**, 20028 (2004).

7. Leuba S. H., Bustamante C., van Holde K. and Zlatanove J. Biophys. J. 74, 2830 (1998).

8. Khorasanizadeh S. *Cell*. **116**. 259 (2004).

9. Masayoshi L. and Smith M.M. *Curr. Opin. Genet. Dev.* **13**, 154-160 (2003).

10. Mellor J. *Mol. Cell.* **19**, 147 (2005).

11. Johnon C. N., Adkins N. L. and Georgel P. *Biochem. Cell Biol.* **83**, 405 (2005).

12. Smith C. L. and Peterson C. L. *Curr. Top. Dev. Biol.* **65**, 115 (2005).

13. Narlikar G. J., Fan H. Y. and Kingston R. E. *Cell*. **108**. 475 (2002).

14. Luger K. and Hansen J. C. *Curr. Opn. in Struct. Biol.* **15**, 188 (2005).

15. Cui Y. and Bustamante C. *Proc. of the Natl. Acad. of Sci.* **97,** 127 (2000).

16. Houchmandzadeh B., Marko J. F., Chatenay D. and Libchaber A. *J. Cell Biol*. **139**. 1 (1997).

17. Pope L. H., Bennink M. L., van Leijenhorst-Groener K. A., Nikova D., Greve J. and Marko J. F. *Biophys. J.* **88**, 3572 (2005).

18. Pope L.H., Bennink M. L. and Greve J. *J. Muscle Res. Cell Motil*. **23**, 397 (2002).

19. Zlatanova J. and Leuba S. H. *J. Mol. Biol*. **331**, 1 (2003).

20. Brower-Toland B. D., Smith C. L., Yeh R. C., Lis J. C., Peterson C. L. and Wang M. D. *Proc. Natl. Acad. of Sci.* **99**, 1960 (2002).

21. Brower-Toland B., Wacker D. A., Fulbright R. M., Lis J. T., Lee Kraus W. and Wang M. D. *J. of Mol. Biol.* **346**, 135 (2005).

22. Horn P. J. and Peterson C. L. *Science.* **297**, 1824 (2002).

23. Leuba S. H., Bustamante C., Zlatanova J. and van Holde K. Biophys. J. 74, 2823 (1998).

24. Gruenbaum Y., Margalit A., Goldman R.D., Shumaker D.K. and Wilson K.L. *Nat. Rev. Mol. Cell Biol.* **6**, 21 (2005).

25. Shumaker D.K., Kuczmarski E.R. and Goldman R.D. *Curr. Opin. Cell Biol.* **15**, 358 (2003).

26. Nickerson J.A., Krockmalnic G., Wan K.M. and Penman S. *Proc. Natl. Acad. Sci. USA.* **94**, 4446 (1997).

27. Dahl K. N., Kahn S. M., Wilson K. L., and Discher D. E., *J. Cell Sci.* **117**, 4779 (2004).

28. Dahl K. N., Engler A. J., Pajerowski J. D. and Discher D. E., *Biophys. J.* **89**, 2855 (2005).

29. Ou-Yang H. D. *Colloid-Polymer Interactions: From fundamentals to practice.* (1999).

30. Valentine M. T., Dewalt L. E. and Ou-Yank H. D. *J. Phys. Condens. Matter.* **8**. 9477 (1996).

31. Nemet, B. A. and Cronin-Golomb M. Measuring microscopic viscosity with optical tweezers as a confocal probe. *Applied Optics*. **42**.1820 (2003).

32. Gruenbaum Y., Margalit A., Goldman R. D., Shumaker D. K. and Wilson K. L., *Nat. Rev. Mol. Cell. Biol.* **6**, 21 (2005).

33. Shumaker D. K., Kuczmarski E. R. and Goldman R. D. *Curr. Opn. in Cell Biol.* **15**, 358 (2003).

34. Karabinos A., Schunemann J., Meyer M., Aebi U. and Weber K. *J. Mol. Biol.* **325**, 241 (2003).

35. Panorchan P., Schafer B. W., Wirtz D. and Tseng Y., *J. Biol. Chem.* **279**, 43462 (2004).

36. Protacio R. U., Li G., Lowary P. T. and Widom J. *Mol. Cell. Biol.* **20**, 8866 (2000).

Appendix

Membrane nanotubule as a probe of the dynamics of DNA self-assembly.

Membrane nanotubules are excellent precursors for nanofabrication since the tubule length and radius can be controlled [1]. The radius of the tubule depends on the membrane tension; hence they can be used as precise templates for nanofabrication. DNA and other conducting molecules adhered onto the membrane tubules are potential candidates for nanowire fabrication. The negatively charged DNA molecules integrate onto the membrane bilayer, with the cationic surfactant molecules acting as counter-ions [2]. A cryo-AFM image of DNA assembled on DTAP membrane bilayers is shown in Figure A.1(a) [3]. X-ray diffraction studies, Cryo-electron microscopy and neutron scattering methods have been used to study the structures of these complexes [4, 5]. Liquid crystalline phases like the DNA intercalated lamellar phases and the inverted hexagonal phases are known to form depending on the DNA and lipid concentrations, as shown in Figure A.1 (b) and (c) [2]. Although DNA-cationic lipid complexes have been studied through bulk experiments, the dynamics of such integration has not been monitored in real time. Atomic force microscope based cantilever has been used to determine the force required for pulling out a DNA molecule adhered onto the cationic membrane bilayer, and the value is ~45pN [6]. We have followed the real time integration of the DNA molecules on membrane nanotubules and consequential changes in the membrane properties due to change in structure.

The nanotubules drawn from the vesicle using the optical trap is used as a sensor of DNA integration. Using the tubule as a handle, we directly monitored the change in its elastic parameters due to DNA integration. 5μl of DNA (Lambda DNA Hind III, 2 #SM101 MBI Fermentas; 0.5 mg/ml, preheated at 95^0C for 5 minutes) was added into the sample well containing the vesicle adhered to the trapped bead. The Lambda HindIII DNA consists of DNA fragments of sizes varying from 125bp (42.5nm in length) to 23.13kbp (7.8μm in length).

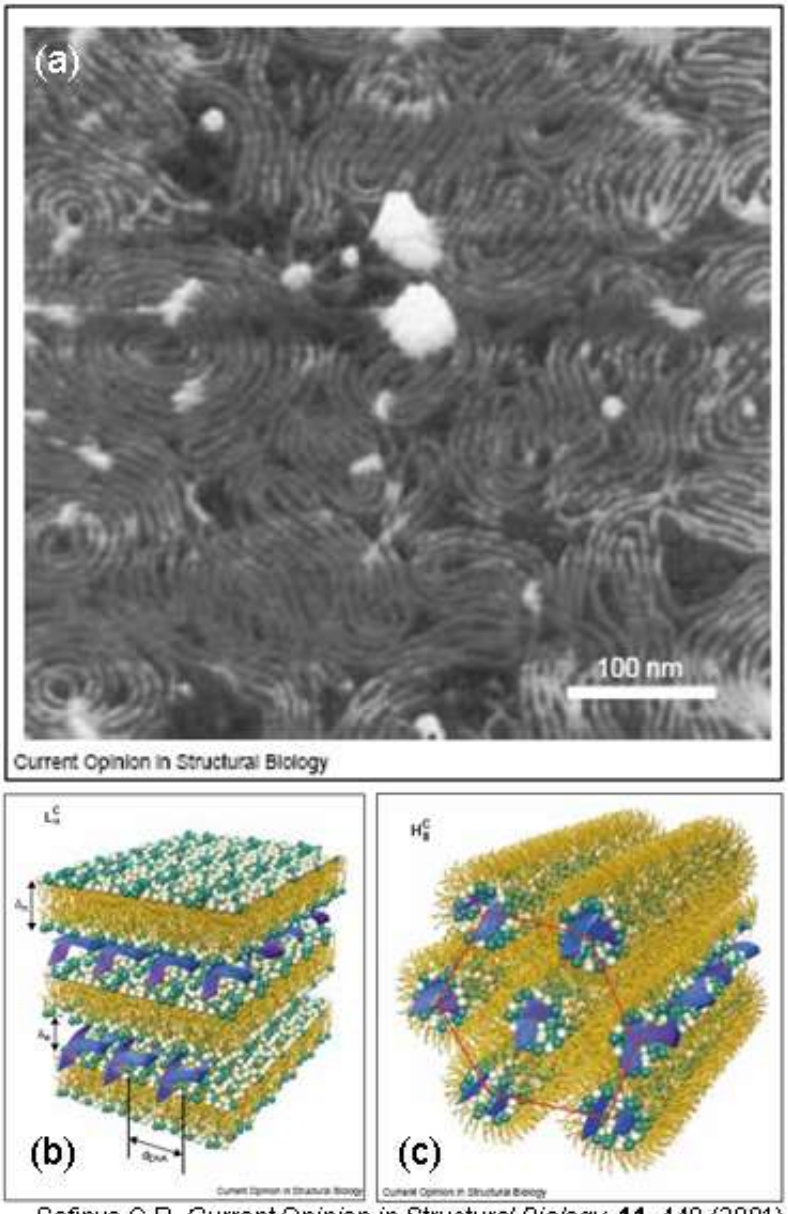

Safinya C.R. *Current Opinion in Structural Biology*. **11**, 440 (2001)

Figure A.1

(a) Cryo-AFM image of DNA assembled on membrane bilayers [2]. (b) and (c) show lamellar and inverted hexagonal phases respectively of DNA-lipid complexes [2]

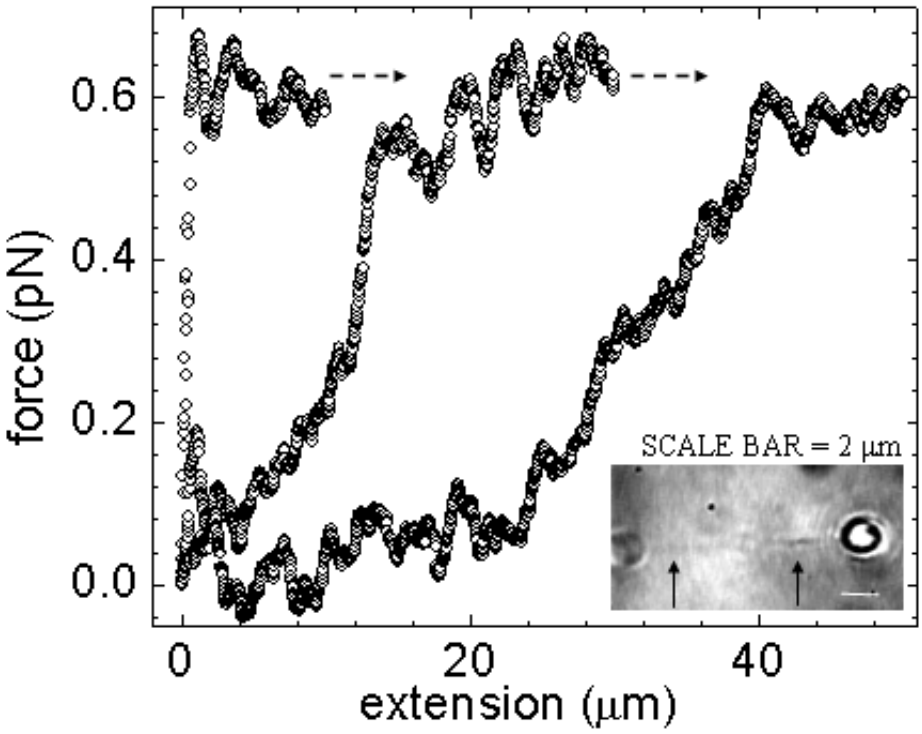

Figure A.2

Force extension curves recorded with DNA assembled membrane tubule showing the onset of entropic response. The three curves show the time evolution (~ 2' interval) of DNA integration on the tubule. Inset to the figure shows the optical image of the tubule pulled out of the vesicle, the assembly of DNA rendering it optically visible. The black arrows mark the tubule. The scale bar in 2μm.

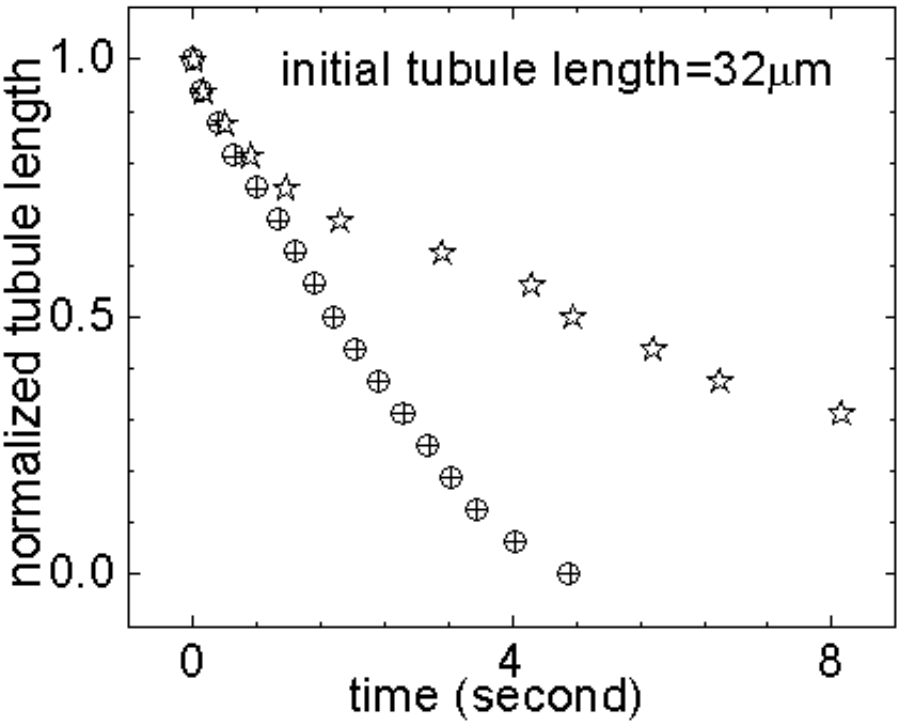

Figure A.3

The recoil of the membrane tubule before and after DNA integration. The recoil curves with DNA are taken after the tubule becomes optically visible. The tubule length is normalized with the length of the tubule before the DNA assembly (32μm).

Force extension curves were then recorded on the same tubule, as a function of time, as shown in Figure A.2. We find that the integration of DNA molecules on the tubule results in the deformation of the membrane as a function of time.

Within about 5' of addition of DNA, the integration of the negatively charged DNA polymer on the membrane vesicle leads to formation of lipid-DNA complexes. The negatively charged DNA molecules integrate onto the tubule, with the cationic surfactant molecules acting as counter-ions. We observe characteristic changes in the tubule formation, as the DNA molecules assemble onto the membrane tubule. The two distinct features of the force extension curve measured before the addition of DNA in the sample well; the initial sharp rise in the force and its saturation are altered (as shown in Figure A.2). As a function of DNA integration, the tubule behaves more as a random coil (similar to that of a DNA polymer). The surfactant molecules are recruited as counter ions to neutralize the charge on the assembled DNA, hence disrupting the fluid like nature of the membrane and also making them optically visible; inset to Figure A.2. In Figure A.3, we plot the recoil of the optically resolved DNA assembled tubule. The long recoil time scales, suggest its entropic nature, which is also revealed in the force extension curves. The membrane pulled out into the tubule fails to integrate back into the vesicle suggesting loss of the fluidic property of the bilayers. The tubule and the vesicle eventually rupture forming DNA-lipid complex, at sufficiently high DNA concentration on the membrane.

We studied the real-time dynamics of DNA self-assembly on tethered membrane nanotubules. We show here that the integration dynamics is independent of the contour length of the DNA molecules. DNA assembly on the tubule is probed by anchoring it to the trapped bead that is held at a constant force by a feedback loop, as shown in Figure A.4. The tubule is extended to ~15μm from the vesicle adhered on the cover slip, where we are in the saturation regime of the force curve and the bead is held at a constant force ~0.3pN. The bead position is continuously monitored on the position sensing quadrant photodiode

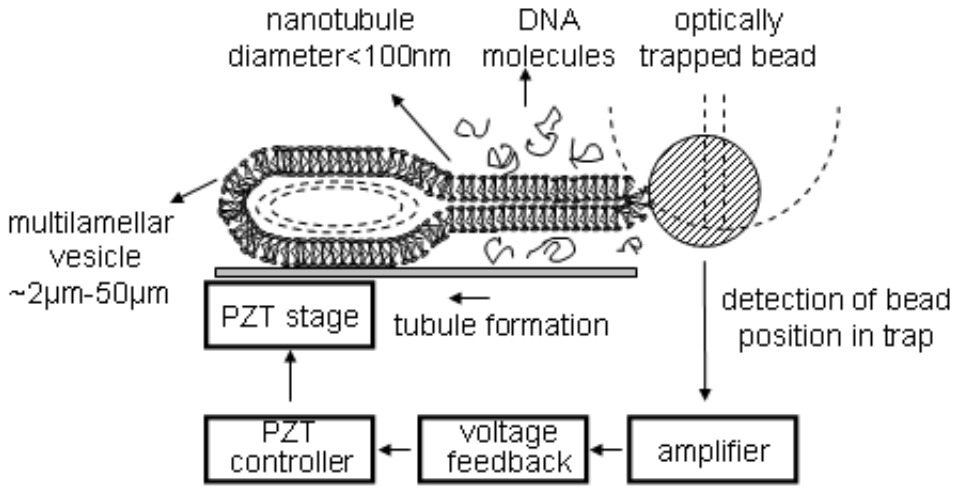

Figure A.4

Schematic of the experiment to measure DNA integration on tubule held at constant force. The optically trapped bead is used to tubulate the vesicle adhered on the cover-slip mounted on the PZT stage. The force of tubulation is monitored using a photosensitive quadrant detector and amplifier. The amplifier output is the feedback to the PZT stage for constant force measurement of DNA assembly.

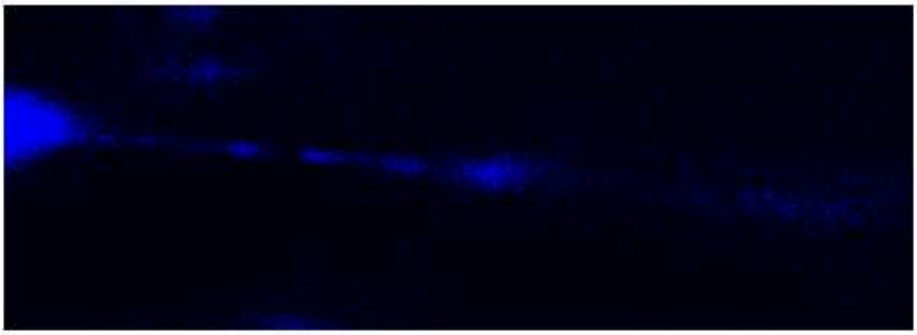

Figure A.5

Fluorescence image of the DNA (stained with YOYO, 1molecule/5bp of DNA).

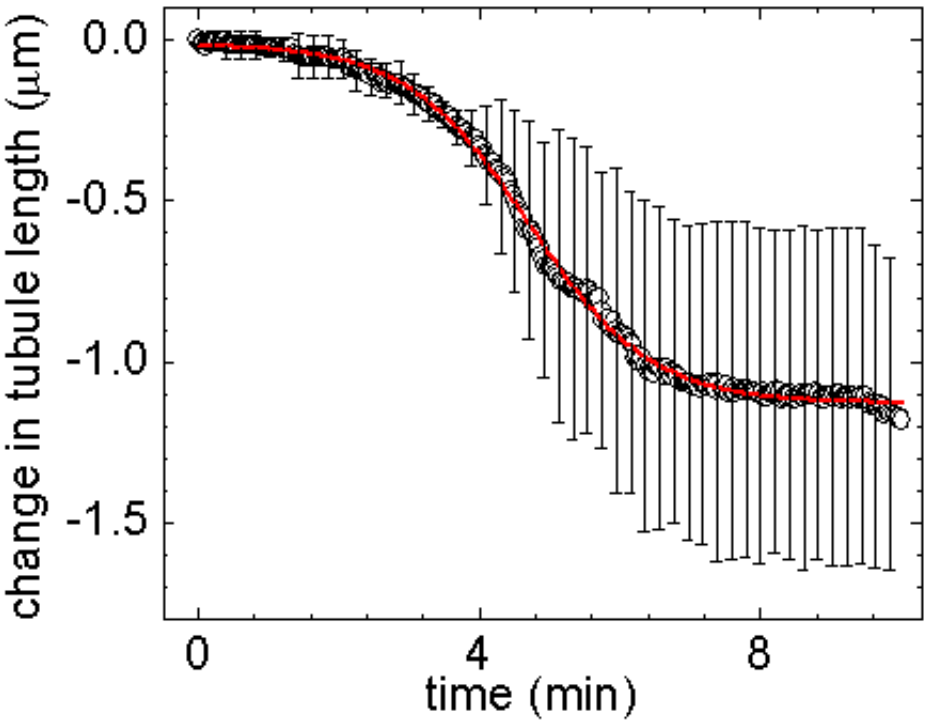

Figure A.6

Plot of the dynamics of DNA self-assembly on the membrane nanotubule as a function of time (recorded using constant force trap measurement). Change in length of the tubule is found to be independent of the size of the DNA molecules (100bp, 5kbp & 48kbp).

using the backscattered red laser. The length of the tubule changes as a consequence of the rupture of the membrane bilayer, due to the condensation of the DNA molecules. This results in an increase in force on the bead, hence a shift in its mean position in the trap. The difference in the two mean positions is the feedback to the PZT stage to compensate for the change in length. Since the trapped bead is a Brownian particle, its mean position in the trap fluctuates and hence the feedback is activated only when the shift in the mean position is greater than four times the standard deviation of the fluctuations. Figure A.5 shows fluorescence image of the DNA assembled on the tubule. The DNA molecules are stained with YOYO dye at a concentration of 1 molecule of YOYO per 5 base pairs of DNA. The DNA molecules nucleate at different points on the tether, and the intensity of each of these nuclei grows with more molecules concentrating at these points, before the tubule breaks.

In Figure A.6 we plot the DNA assembly curves which are similar (and fall within the range shown in the figure) for 100bp, 5kbp and 48kbp DNA sizes. There is an initial slow rate of decrease in length for about 4min, in this phase all the sizes show the same rate. During the time from 4min to 7min the rate is exponential over which the length decreases by ~1μm before it saturates. The exponential rate of decrease continues for much longer lengths (up to 7μm) in some cases. The condensing DNA molecules recruit the lipid molecules of the tubule membrane bilayer to neutralize their charge and release the counter-ions. DNA, being a negatively charged polymer with a high charge density, assembles on cationic membrane bilayers. This process, driven by electrostatic interactions, is a self-assembling process. The increase in entropy, due to counter-ion release as a result of the DNA condensation on the membrane, more than offsets the decrease in entropy due to the DNA condensation itself. The cationic surfactant molecules of the vesicle neutralize the charge on the DNA and hence coat the DNA. With increase in the DNA concentration on the membrane more surfactant molecules are pulled out of the bilayer. The membrane bilayer is slowly ruptured resulting in the decrease in the tubule length as shown in Figure A.6. Eventually the vesicle is completely ruptured and we observe DNA-lipid complexes under the microscope. The plots show that the dynamics of the assembly, at its onset and during the rapid decrease in length, is independent of the size of the DNA molecules. With time the variation between the

curves, obtained for different DNA sizes on different vesicles, increases probably due to the variability in the vesicles. The initial slow phase of decrease in tubule length is when the DNA molecules nucleate at different points along the tubule. When the nuclei start to grow, there is a rapid decrease in length of the tubule, after which the rate of decrease saturates and eventually the tubule breaks. The assembly curves fit to a sigmoidal curve, with a variation in the rates in the exponential regime. For the sigmoidal fit shown in the Figure A.6, the assembly rate ~0.3μm/s.

References

1. Evans E., Bowman H., Leung A., Needham D. and Terrell D. *Science.* **273**, 933 (1996).

2. Safinya C. R. *Curr. Opi. Struct. Biol.* **11**, 440 (2001).

3. Mou J., Czajkowsky D. M., Zhang Y. and Shao Z. *FEBS Lett.* **371**, 279 (1995).

4. Raedler J. O., Koltover I., Salditt T. and Safinya C. R. *Science.* **275**, 810 (1997).

5. Huebner S., Battersby B. J., Grimm R. and Cevc G. *Biophys. J.* **76**, 3158 (1999).

6. Cai Xian-E. and Yang J. *Biophys. J.* **82**, 357 (2002).